

Aerosol layer height (ALH) retrievals from oxygen absorption bands: Intercomparison and validation among different satellite platforms, GEMS, EPIC, and TROPOMI

5 Hyerim Kim¹, Xi Chen¹, Jun Wang^{1,2}, Zhendong Lu², Meng Zhou², Gregory R. Carmichael¹, Sang Seo Park³, Jhoon Kim⁴

¹Department of Chemical and Biochemical Engineering, Center for Global and Regional Environmental Research, Iowa Technology Institute, The University of Iowa, Iowa City, 52242, USA

²Interdisciplinary Graduate Program in Informatics, The University of Iowa, Iowa City, 52242, USA

10 ³School of Urban and Environmental Engineering, Ulsan National Institute of Science and Technology (UNIST), Ulsan 689-798, Republic of Korea

⁴Department of Atmospheric Sciences, Yonsei University, Seoul 03722, South Korea

Correspondence to: Xi Chen (xi-chen-4@uiowa.edu); Jun Wang (jun-wang-1@uiowa.edu)

Abstract.

15 Aerosol vertical distribution is crucial for assessing surface air quality and the impact of aerosols on climate. Although aerosol vertical structures can be complex, assuming a shape of the aerosol vertical profile enables the retrieval of a single parameter, aerosol layer height (ALH), from passive remote sensing measurements. In this study, we compare ALH products retrieved using oxygen absorption measurements across multiple satellite platforms: the Geostationary Environment Monitoring Spectrometer (GEMS) focusing on Asia, the Earth Polychromatic Imaging Camera (EPIC) in deep space, and the polar-orbiting TROPOspheric Monitoring Instrument (TROPOMI). All analyses are conducted for selected “golden days”, which represent ideal viewing conditions for typical dust and smoke cases. Adjustments have been made to standardize the definitions of ALH among different products, ensuring an apple-to-apple comparison. We validate these products using spaceborne lidar (CALIOP) measurements. Compared to CALIOP ALH, both EPIC and TROPOMI ALH show a high correlation coefficient ($R > 0.7$) but an overestimation of ~ 0.8 km. GEMS ALH displays minimal bias (0.1 km) but a slightly lower correlation ($R =$
20 0.64). When comparing GEMS ALH to TROPOMI and EPIC, GEMS shows a narrower range and correlation coefficients are both below 0.4 ($R < 0.4$). Categorizing GEMS retrievals with an ultraviolet aerosol index (UVAI) ≥ 3 improves the agreement with CALIOP. GEMS ALH demonstrates a narrower range and lower mean value compared to EPIC and TROPOMI, with improved correlation for UVAI ≥ 3 . Considering the significant role of aerosol optical depth (AOD) in ALH retrieval, we found that GEMS AOD at 680 nm correlates well with AERONET AOD ($R \approx 0.9$) but shows a negative bias of -0.2. In dust
30 cases, EPIC and TROPOMI tend to overestimate AOD by 0.33 and 0.23, respectively. Furthermore, diurnal variations of ALH from GEMS and EPIC is shown. Finally, we analyze a dust and a smoke case in detail to explore ALH variation during plume transport using multiple data sources.

1 Introduction

Atmospheric aerosols influence the Earth’s energy budget and climate system by absorbing and scattering solar and terrestrial
35 radiation (Wang and Christopher, 2003). The aerosol vertical distribution is one of the most important factors determining the aerosol radiative effects (Zhang et al., 2013). The altitude of absorbing aerosols such as dust and smoke affect the vertical distribution of radiative heating and modify the stability of the atmosphere (Babu et al., 2011; Koch and Del Genio, 2010; Wendisch et al., 2008; Wang and Christopher, 2006). When aerosols are lifted to high altitudes in upper troposphere and lower stratosphere, they can have longer residence times and transport over longer distance, influencing global radiative energy
40 budget (Christian et al., 2019; Peterson et al., 2014). Aerosol vertical distribution influence the derivation of aerosol optical

properties, such as aerosol optical depth (AOD) and single scattering albedo (SSA) in the ultra-violet (UV) spectrum where the top-of-atmosphere (TOA) radiance is also sensitive to the vertical variation of aerosols (Torres et al., 1998). Furthermore, estimates of surface concentration of particulate matter (PM) from the total columnar aerosol loading or AOD requires the knowledge or assumption about aerosol vertical distribution (Wang and Christopher, 2003). Aerosol profile is controlled by
45 diverse processes, such as convective transport, in-cloud scavenging, particle growth by condensation, biomass burning emission and injection height, boundary layer mixing and more, depending on different sources and aerosol properties (Wang et al., 2006; Kipling et al., 2013; Yang et al., 2013; Kipling et al., 2016). Due to the complexity in these processes and lack of temporal and spatially resolved information, aerosol vertical profile has large uncertainty and diversity in chemical transport models (Wang et al., 2013; Yang et al., 2013; Koffi et al., 2016). Therefore, measuring accurate aerosol vertical distribution
50 is still a challenge but critical in many research areas.

Satellite remote sensing techniques are effective for globally monitoring aerosol vertical profiles. Active satellite remote sensing, especially space-borne lidar such as Cloud-Aerosol Lidar with Orthogonal Polarization (CALIOP), on board with the Cloud-Aerosol Lidar and Infrared Pathfinder Satellite Observation (CALIPSO) platform, acquires backscatter profiles and
55 retrieves aerosol extinction profiles with high vertical resolution (Winker et al., 2013). However, the global coverage of CALIOP is less than 0.2% due to its narrow swath and wide gaps between orbits. In contrast, the larger spatial coverage of passive remote sensing measurements overcomes this shortcoming. With the retirement of CALIPSO in August 2023, passive remote sensing will become the only routine technique accessible for the public at present, from space for filling the data gap of measuring aerosol vertical distribution before next lidar dedicated to measure aerosols are launched into space. However,
60 only limited information for aerosol extinction vertical profile can be obtained in passive remote sensing due to the need for multiple assumptions regarding surface and aerosol properties in the retrieval process (Geddes and Bösch, 2015; Rao et al., 2022). Several parameters, including spectral coverage, radiance, polarization, spectral resolution, signal-to-noise ratio (SNR), and the number of viewing angles, can influence the information content and retrieval uncertainties of aerosol profiles (Chen et al., 2021a). Choi et al. (2021) found that the degrees of freedom for signal (DOFS) for a single California Laboratory for
65 Atmospheric Remote Sensing Fourier Transform Spectrometer (CLARS-FTS) measurement becomes sufficient to retrieve three key aerosol parameters—AOD, aerosol peak height, and aerosol layer thickness in the planetary boundary layer (PBL)—when adding a high spectral resolution (with a full-width half-maximum of 3 cm^{-1} or better), polarimetric measurements with SNR of at least 212, and radiance measurements with SNR of 300 for both oxygen (O_2) A and $^1\Delta$ bands. While satellite instruments, such as TROPOMI and EPIC, lack adequate DOFS on an individual basis, their integration with joint radiometric
70 and polarimetric measurements of the O_2 A and B bands—with a resolution of 3 cm^{-1} , a radiance SNR of 500, and a polarization SNR of 353—acquired at three viewing angles, enables the simultaneous retrieval of the three aerosol parameters (Choi et al., 2021).

Hence, many algorithms have been developed to extract a single piece of information regarding aerosol vertical distribution,
75 with a primary emphasis on aerosol layer height, which approximates the altitude of aerosols of a presumed aerosol vertical profile. Passive sensing techniques to retrieve aerosol layer height (ALH) information include stereo photogrammetry, polarimetric techniques in UV-VIS spectrum, infrared (IR) technique, and atmospheric oxygen (O_2) absorption (Pierangelo et al., 2004; Muller et al., 2007; Zeng et al., 2008; Vandenbussche et al., 2013; Wu et al., 2016; Xu et al., 2018; Kim et al., 2023). Not only different physical theories are these techniques based on, but each product has different definitions of ALH and
80 parameterizations of aerosol profiles, including aerosol optical central height (AOCH), aerosol effective height (AEH), etc. Part of this study will analyse how the assumption of the shape of aerosol vertical profiles in the retrieval may lead to inherent differences in the retrieval product. Beyond this theoretical analysis, this study mainly focuses on evaluating three ALH data

products retrieved from three different satellite sensors that detect the TOA measurements in various O₂ absorption from visible to near-infrared bands.

85

Aerosols positioned at lower altitudes cause light to travel a longer path, resulting in increased absorption by O₂ molecules along the extended path (Ding et al., 2016; Xu et al., 2019). Consequently, the amount of scattered radiation received by satellites decreases as aerosol layer decreases in altitude. Kokhanovsky and Rozanov (2010) retrieved the top height of dust layer by fitting spectral TOA reflectance measurements from the O₂ A band (around 760 nm) of the Scanning Imaging
90 Absorption spectroMeter for Atmospheric CHartographY (SCIAMACHY). Similarly, the official operational ALH product of TROPOspheric Monitoring Instrument (TROPOMI) uses measurements of the O₂ A band to retrieve the centroid pressure or height of a presumed single aerosol layer (Nanda et al., 2020). However, retrieving ALH information over land, including areas with vegetation and soil surfaces, from the O₂ A band presents challenges. This is because the TOA reflectance in this band is dominated by high surface reflectance instead of aerosol scattering. Consequently, TOA reflectance becomes less
95 sensitive to ALH, and errors in surface reflectance contribute to significant uncertainties in ALH retrieval (Xu et al., 2019).

Despite the weaker oxygen absorption in the O₂ B band (near 688 nm) than in the O₂ A band, the surface reflectance is significantly lower in the O₂ B band across all land types, which proves advantageous for aerosol retrieval. Based on this principle, (Xu et al., 2017; Xu et al., 2019) have developed a retrieval algorithm that use measurements from both O₂ A and B
100 bands, applying it to observations from the Earth Polychromatic Imaging Camera (EPIC)/Deep Space Climate Observatory (DSCOVR) to produce a product known as aerosol optical central height (AOCH). Based on this algorithm, with several adjustments, an enhanced algorithm was developed and implemented in hyperspectral measurements from TROPOMI (Chen et al., 2021) as TROPOMI Aoch. In comparison with the operational TROPOMI ALH product, which shows a bias of 2 km over land, TROPOMI Aoch shows a bias of approximately 0.5 km over both ocean and land (Chen et al., 2021b; Nanda et al., 2020). Hence, in the context of this study, we employ TROPOMI Aoch retrieved through the combined utilization of the
105 O₂ A and B bands, favoring it over the operational TROPOMI ALH product retrieved solely from the O₂ A band.

Furthermore, oxygen-dimer (O₂-O₂) absorption bands exhibit sensitivity to ALH similar to O₂ absorption bands. Aimed to observe from 300 to 500 nm range, the Geostationary Environment Monitoring Spectrometer (GEMS) can measure radiation
110 across multiple O₂-O₂ absorption bands, including 340, 360, 380 and 477 nm, with 477 nm found to be the most sensitive to the ALH due to its largest O₂-O₂ absorption (Chimot et al., 2017; Cho et al., 2024; Kim et al., 2020; Park et al., 2016). GEMS provides an aerosol layer height product, termed aerosol effective height (AEH), retrieved from the 477 nm O₂-O₂ absorption band. This algorithm has been applied in the Ozone Monitoring Instrument (OMI) measurements, and recently been evaluated with CALIOP, revealing negligible bias and a standard deviation of 1.4 km in the AEH difference across the GEMS
115 observation domain from January to June 2021 (Park et al., 2024; Park et al., 2016).

The three oxygen-related bands, namely, O₂-O₂ 477 nm band, and the O₂ A and B bands, have differences in terms of oxygen absorption strength and surface reflectance, leading to their diverse sensitivities to ALH. Hence, comparing retrievals from different O₂ absorption bands can offer valuable insights into their respective advantages and limitations in ALH retrieval.
120 This motivates us to validate three different satellite ALH products, GEMS, EPIC and TROPOMI, using CALIOP three-dimensional aerosol extinction product and conduct intercomparisons among them. While the validation of diurnal variations in ALH currently remains challenging, leveraging GEMS' hourly products alongside the close-hourly EPIC global retrievals allows us to conduct comparative analyses with the available data at hand.

125 Additionally, evaluation of ALH retrievals should consider the context of other retrieval parameters, such as AOD and UV
aerosol index (UVAI). UVAI quantifies the difference between measured and calculated near-UV spectral dependence, with
values near zero indicating an aerosol-free atmosphere or the presence of non-absorbing aerosols and clouds, while positive
values are associated with UV-absorbing aerosols like carbonaceous aerosols, volcanic ash, and desert dust (Torres et al.,
2007). Accurate retrieval of ALH requires reliable retrieval of AOD since the retrieval sensitivity is strongly dependent. Park
130 et al. (2016) showed higher sensitivity of oxygen-dimer (O_4) slant column density to aerosol effective height at 477 nm with
higher AOD. Xu et al. (2019) showed the sensitivity of Differential optical absorption spectroscopy (DOAS) ratios—the ratio
of TOA reflectance between the absorption band and the continuum band—to ALH is enhanced for lower surface reflectance
and higher AOD. Moreover, the sensitivity of UVAI to ALH, along with their correlation, rises with increasing AOD levels
(Xu et al., 2019; Xu et al., 2017). Therefore, we evaluate AOD with AERONET, cross-compare AOD and UVAI products
135 from different platforms as well as the relationship of ALH between products with different UVAI to see its impact.

Considering that the spatial coverage of CALIOP is limited, we carefully selected “golden” cases where dust and smoke events
favor the retrievals from all three sensors. This selection can maximize the signal to noise ratio for ALH retrieval, and hence,
the evaluation can shed light on the future improvement to bring the closure of various types of retrievals. Note that these
140 conditions may differ from those observed on non-selected days. In addition to pixel-by-pixel comparison of these passive
satellite products, they are also assessed with CALIOP aerosol extinction profiles along CALIOP’s track. We provide a detailed
comparison with CALIOP profiles for a dust and a smoke plume case. This paper outlines the data and comparison approach
in section 2, followed by the comparison results for all data used in this study in section 3. Section 4 shows the investigation
of the ALH variation during transport for selected dust and smoke cases. Lastly, conclusions and discussions are provided in
145 section 5.

2 Data and methodology

The ALH products compared in this study share similarities in that they are all derived using oxygen (or its dimer) absorption
bands and assume the same aerosol vertical profile shape. However, there are distinct variations in the specifics of each
algorithm, including the definition of ALH, which may result in inherent differences in ALH retrievals. In section 2.1, we first
150 introduce the characteristics of each passive product, providing some details of each retrieval algorithm, as well as presenting
the retrieval performance from previous studies. The difference of ALH definitions is compared in section 2.2. Lastly, the
approaches for comparing ALH data and evaluating them with ground-based observations or active measurements are
illustrated in section 2.3.

2.1 Satellite data

2.1.1 GEMS

From a geostationary orbit about 36000 km above the equator, GEMS provides hourly measurements over Asia within the
latitudes of 5°S to 45°N and the longitudes of 80°E to 152°E (Kim et al., 2020). Given the lower SNR in the morning due to
large solar zenith angle (SZA), GEMS only scan the east half of the field of regard, leading to less products available over
160 west region. The total amount of hourly products in each day also depends on the SZA in different seasons. The spatial
resolution of GEMS products is 3.5×8 km (north-south and east-west) at Seoul, South Korea.

GEMS offers two products describing aerosol altitude, AEH and aerosol loading height, each derived from different
algorithms. GEMS aerosol loading height, included in the level 2 GEMS aerosol product (L2AERAOD), employs an optimal
estimation method, incorporating measurements at six wavelengths, including the O_2 – O_2 band at 477 nm (Cho et al., 2024;

165 Kim et al., 2018). In contrast, GEMS AEH algorithm uses the sensitivity of the O₂-O₂ band to the ALH similar to TROPOMI and EPIC using O₂ A and B bands, which will be discussed in the following subsection. Therefore, this study specifically focuses on analyzing GEMS AEH version 2.0.

GEMS AEH is retrieved using the O₂-O₂ slant column density (SCD) at 477 nm with a look-up table (LUT) approach adopting aerosol types, AOD, and SSA at 550 nm from L2AERAOD, and surface reflectance from the GEMS standard product for surface reflectance (Park et al., 2024). Three aerosol types were classified using UVAI and the Visible Aerosol Index (VisAI), which, similar to UVAI but with visible channels, categorizes aerosols into highly absorbing fine (HAF), dust, and non-absorbing (NA) aerosols. NA aerosols are selected when UVAI yields a negative value, the dust type is determined when both UVAI and VisAI are positive, and HAF is selected when UVAI is positive, but VisAI is negative (Cho et al., 2024). For LUT generation, aerosols are assumed to be spherical due to the computationally intensive spectral binning method, and the particle size distribution, refractive index, and fine mode fraction for each aerosol type are derived from the global Aerosol Robotic Network (AERONET) inversion climatology (Cho et al., 2024).

175 Cho et al. (2024), validated GEMS AOD at 443 nm against AERONET data across the entire GEMS domain from November 1, 2021, to October 31, 2022. They found the total GEMS AOD showed a R value of 0.792, a root mean square error (RMSE) of 0.227, and a mean bias error (MBE) of 0.038. Park et al. (2024) retrieved and validated GEMS AEH with CALIOP AEH. 180 The differences in AEH between GEMS and CALIOP for dust plume cases were -0.07 ± 1.09 and -0.11 ± 1.27 km, with 53.8% and 72.9% of all pixels showing differences less than 1.0 and 1.5 km, respectively. Moreover, during the period from January to June 2021, they observed an average AEH difference of -0.03 km.

2.1.2 EPIC / DSCOVER

185 Carried on the DSCOVER spacecraft at the Sun-Earth Lagrange-1 point (L1) 1.5 million km from the Earth, EPIC captures the image for sunlit disk of Earth every 60-100 mins per day. As a result, EPIC monitors the half globe close-hourly, rendering a full disk of 2048×2048 pixels at the spatial resolution of size of 12 km at the Earth surface (Marshak et al., 2018). With 10 narrow channels, EPIC detects the Earth-reflected solar radiance from ultraviolet, visible, to near-infrared (NIR) bands, including both O₂ A and B bands. The fact that the lower surface reflectance in O₂ B band than O₂ A band over land (Xu et al., 2019) motives us to use O₂ B band to improve the ALH retrievals that use the O₂ A band solely. Xu et al. (2017) developed an algorithm to retrieve aerosol optical central height (AOCH) from EPIC measurements in O₂ A and B bands at the first time and applied it for dust plumes in Atlantic Ocean. Later, Xu et al. (2019) added a smoke model in the LUT and applied it into several smoke plume cases over the Hudson Bay-Great Lakes area in North America. They found that over 77% collocated AOD pairs fell within an uncertainty envelope of $\pm (0.05 + 0.1 \text{ AOD})$, with a coefficient of determination (R²) of 0.54. Based on this algorithm, Lu et al. (2021) updated the calibration of EPIC level 1 data and analysed the EPIC AOCH for U.S. smoke plumes during 2020 California big wildfires. The validation of EPIC AOCH against the extinction-weighted AOCH from lidar observations, CALIOP, in these papers show a high level of accuracy, with a correlation coefficient of 0.885 and a RMSE of 0.92 km for absorbing aerosols. The surface reflectance data involves two sources: land surface reflectance is obtained from the MODIS surface bi-directional reflectance climatology, while water surface reflectance is derived from the GOME-2 surface Lambert-equivalent reflectivity (LER) database. Furthermore, a new LUT developed specifically for dust plumes in the East Asian region, based on multi-year AERONET inversion products, has been 200 incorporated, as detailed in Lu et al. (2023).

2.1.3 TROPOMI / S5P

205 TROPOMI on board the Copernicus Sentinel-5 Precursor satellite was launched in October 2017 to measure solar radiation reflected by Earth from UV to shortwave infrared (SWIR) bands including many trace gases absorption bands and the surface and aerosol information. Flying on a polar satellite, TROPOMI provides global atmospheric components products on a high spatial resolution, $5.5 \text{ km} \times 3.5 \text{ km}$ (improved from $7 \text{ km} \times 3.5 \text{ km}$ since August 2019) once every day.

TROPOMI measures both O₂ A and B absorption bands, yet its official ALH product utilizes solely the O₂ A band measurements in its retrieval algorithm (Nanda et al., 2020). Chen et al. (2021b) developed an alternative algorithm suitable for TROPOMI data, enabling AOCHE retrieval using both O₂ A and B bands. This approach draws upon the EPIC AOCHE retrieval algorithm by Xu et al. (2019), employing the same look-up table (LUT) and least square method to optimize AOCHE from the ratio of O₂ absorption to its nearby continuum band. Enhancements include spectral resolution convolution into multiple narrow channels, a new cloud mask, and dust/smoke classification, with results reported in a standard latitude-longitude grid ($0.05^\circ \times 0.05^\circ$). Comparative analysis reveals that the AOCHE exhibits approximately a 0.5 km bias over both ocean and land, contrasting with the 2 km bias observed in the operational ALH product from TROPOMI (Chen et al., 2021b; Nanda et al., 2020). Consequently, this study employs TROPOMI AOCHE retrieval data, as previously highlighted in the introduction. Furthermore, the new LUT developed for Asian dust plumes in EPIC retrievals has been integrated into the algorithm for application in East Asia. The surface reflectance data is the same used in the EPIC retrieval algorithm. The operational TROPOMI level 2 UVAI product (Stein Zweers, 2022) is used to retrieve only pixels covered by absorbing aerosols with UVAI greater than 0.5.

2.2 Comparison of ALH Definitions

GEMS, TROPOMI, and EPIC algorithms all operate under the assumption that quasi-Gaussian vertical distribution of aerosol extinction described by parameters of loading, peak height (H), and half width parameter at half maxima (η) fixed at 1 km. The assumption of a 1 km half width is grounded in typical Lidar observations for dust and smoke aerosols, as indicated by Reid et al. (2003). This value has also been used in the retrieval of AOD from UV observations by both the Total Ozone Mapping Spectrometer (TOMS) and OMI, as emphasized in the work by Torres et al. (1998). Presently, it is widely accepted as a standard parameter value, evident in products presented in this study. The aerosol extinction profile where z is the altitude with respect to surface can be expressed by a generalized distribution function as specified in Eq. (1):

$$\beta(z) = W \frac{\exp(-\sigma_H |z - H|)}{[1 + \exp(-\sigma_H |z - H|)]^2} \quad \text{Eq. (1)}$$

where H is the altitude with peak aerosol extinction, W is normalization constant related to the columnar loading, and σ_H is defined as: $\sigma_H = \ln(3 + \sqrt{8})/\eta$ (Spurr and Christi, 2014). However, ALH is a general term to describe the altitude of aerosol layer, while the definition of the retrieved ALH varies by algorithm. EPIC and TROPOMI defined their retrieved ALH as H in Eq. (1) and called AOCHE (Chen et al., 2021b; Lu et al., 2023; Lu et al., 2021; Xu et al., 2019; Xu et al., 2017). GEMS AEH is defined as the altitude above which the aerosol extinction is the $1/e$ of total columnar AOD, as described in Eq. (2):

$$\frac{\int_0^{AEH} \beta(z) dz}{\int_0^{TOA} \beta(z) dz} = 1 - e^{-1} \quad \text{Eq. (2)}$$

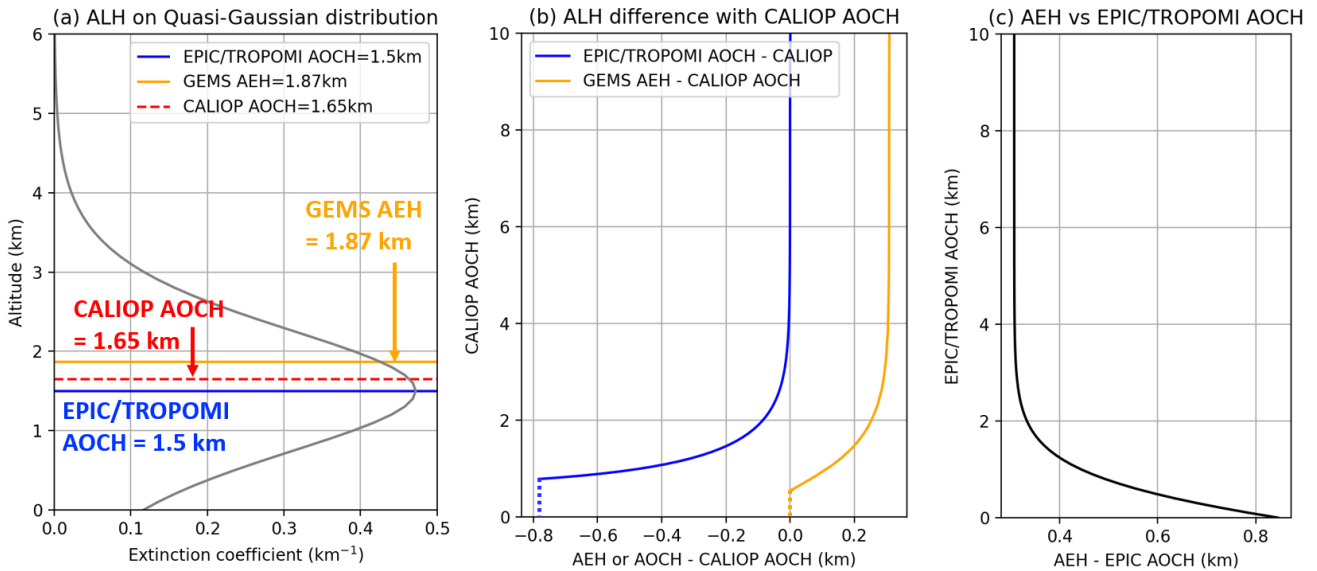
240 In addition, AOCHE retrieved from EPIC and TROPOMI O2AB-UI is relative to geographic (ground) surface, whereas GEMS
 AEH is relative to sea level. Henceforth, for simplicity and consistency, the term ALH will be used to refer to all aerosol height
 products used in this study, including GEMS AEH, TROPOMI AOCHE, and EPIC AOCHE. To validate retrievals from passive
 remote sensing with lidar data, the optical depth weighted heights derived from CALIOP 5 km level 2 aerosol extinction profile
 product at 532 nm following previous studies are used (Chen et al., 2021b; Lu et al., 2023; Lu et al., 2021; Xu et al., 2019).
 245 We define CALIOP AOCHE as the optical depth weighted height, as specified in Eq. (3):

$$AOCH_{CALIOP} = \frac{\sum_{i=1}^n \beta(z_i) \Delta z_i z_i}{\sum_{i=1}^n \beta(z_i) \Delta z_i} \quad \text{Eq. (3)}$$

where $\beta_{ext,i}$ represents the 532 nm aerosol extinction coefficient at vertical level i with an altitude of z , while Δz_i denotes the
 thickness of the vertical layer i .

250 The comparison of different definitions of ALH for the same aerosol vertical distribution is shown in Fig. 1. In an exemplified
 aerosol extinction profile with EPIC or TROPOMI AOCHE at 1.5 km, CALIOP AOCHE stands higher at 1.65 km, with GEMS
 AEH being the highest at 1.87 km (Fig. 1a). The difference between EPIC/TROPOMI and CALIOP AOCHE decreases as
 AOCHE increases, ultimately disappears when CALIOP AOCHE reaches approximately 4 km and beyond. When CALIOP
 AOCHE is below ~ 1 km, EPIC/TROPOMI AOCHE can be as large as 0.5 km lower than CALIOP. GEMS AEH exhibits a larger
 255 difference compared to CALIOP AOCHE for higher AOCHE, and this difference remains relatively constant at approximately
 0.3 km for altitudes above ~ 3 km. Figure 1c illustrates that the difference between GEMS AEH and EPIC/TROPOMI AOCHE
 can reach around 0.8 km near the surface. However, this difference decreases as AOCHE increases, ultimately reaching 0.1 km
 for altitudes above ~ 3 km. In our further comparison of ALH, we count for these inherent differences by converting one
 definition to another to ensure consistency.

260



265 **Figure 1. Comparison of ALH definition (GEMS, EPIC, TROPOMI, and CALIOP).** (a) Relative heights within the quasi-Gaussian
 distribution when EPIC/TROPOMI AOCHE is 1.5 km. (b) Difference between ALH from passive satellite with CALIOP AOCHE.
 Note that EPIC/TROPOMI AOCHE is depicted as dotted vertical lines when it becomes negative below a specific CALIOP AOCHE.
 (c) Difference between GEMS AEH and EPIC/TROPOMI AOCHE definitions with respect to the altitude of EPIC/TROPOMI
 AOCHE.

2.3 Comparison Approach

270 Given the availability of EPIC/TROPOMI retrievals for absorbing aerosols, we focus our comparison on a selection of “golden
 days” characterized by ideal viewing conditions for dust and smoke cases, excluding cloud-covered areas, as observed within
 GEMS field of regard from 2021 to 2023. These selected days are listed in Table 1 and correspond to the study domain depicted
 in Fig. 2. Classification of dust and smoke cases is determined by the predominant aerosol type identified in the CALIOP lidar
 data. Although EPIC products have similar temporal resolution to GEMS, observations over the research domain vary from 3
 275 to 8 per day depending on the solar geometry. Flying on a polar orbit, TROPOMI only observed the whole globe once each
 day, but depending on the latitude of each case, TROPOMI ground track may overlap, which can lead to the possibility of two
 TROPOMI observations for some cases. Considering the differences in spatial and temporal resolutions among these three
 products, we first resample the GEMS product to TROPOMI and EPIC spatial resolution using the pixel area weighted method,
 and then linearly interpolate the GEMS product with time to match the observation time for the paired TROPOMI and EPIC
 280 data (Wang et al., 2020).

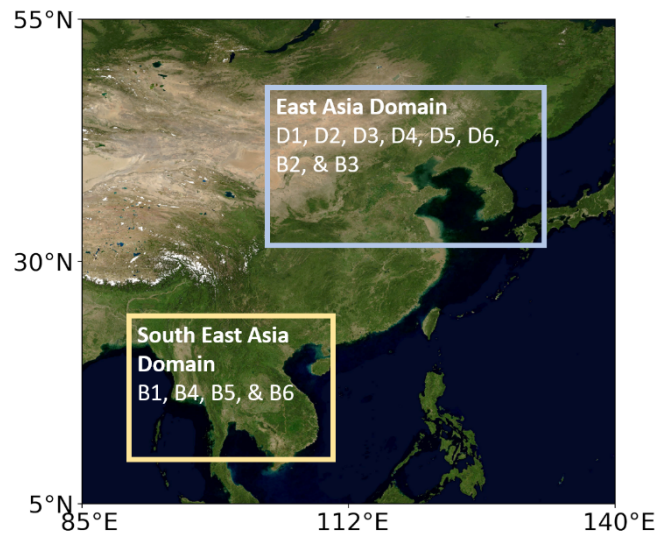


Figure 2. Study domains and cases. "D" represents dust cases, while "B" represents smoke cases ("B" for biomass burning). See Table 1 for more information. Map from Blue Marble: Next Generation from NASA Earth Observatory.

285 **Table 1. Case study dates and the number of observations of each sensor for each domain.**

Case no.	Date	Domain	Number of orbits (or granules)		
			GEMS	TROPOMI	EPIC
D1 ^a	2021-03-28	East Asia	7	2	4
D2	2021-04-26	East Asia	8	2	7
D3	2022-04-10	East Asia	8	2	5
D4	2023-03-10	East Asia	7	2	3
D5	2023-05-19	East Asia	8	2	8
D6	2023-05-20	East Asia	8	2	7
B1	2021-03-31	Southeast Asia	6	1	5
B2	2021-08-10	East Asia	8	1	8
B3	2021-08-11	East Asia	6	2	8
B4	2022-04-09	Southeast Asia	8	2	5
B5	2023-03-26	Southeast Asia	6	1	5
B6	2023-04-17	Southeast Asia	8	1	4

^a: The initial “D” means dust case and “B” represents smoke case from biomass burning.

UVAI data from GEMS, EPIC, and TROPOMI are also cross compared as UVAI is used in all retrieval algorithms. The ALH comparison and validation for different GEMS UVAI is conducted to analyze the possible distinction of GEMS AEH retrieval accuracy for different UVAI values. Furthermore, as the accuracy of each AOD product also influences corresponding ALH retrieval, AOD will be validated by the ground-based AERONET inversions. When matching satellite pixels with ground sites, we consider the number of valid satellite retrievals within a 0.2° radius around AERONET sites. If the number of valid retrievals exceeds 30% of the total number of pixels, we compute the mean value of these retrievals and compare it with the corresponding AERONET AOD. The AERONET AOD is averaged for a period of 30 minutes before and after each satellite observation, aligning with the satellite overpass time (or observation time for GEMS). Furthermore, we only include satellite data points with a spatial standard deviation less than 0.3 to ensure spatial consistency in the comparison. Since TROPOMI and EPIC AOD are retrieved at 680 nm, whereas GEMS AOD is retrieved at 443 nm, we estimate GEMS AOD at 680 nm from its AOD at 443 nm. This estimation is based on a combination of aerosol type (dust, HAF, NA) for each pixel and the Angstrom exponent (440 nm – 677 nm) from the GEMS aerosol model corresponding to the aerosol type (Kim et al., 2018). When co-locating passive satellite products with CALIOP pixels along the track, we employ a similar approach to the comparison with AERONET. This involves calculating the distance from the center of the CALIPSO ground track within a range of 0.2° and adjusting the threshold for valid retrieval to exceed 30%

3 Results

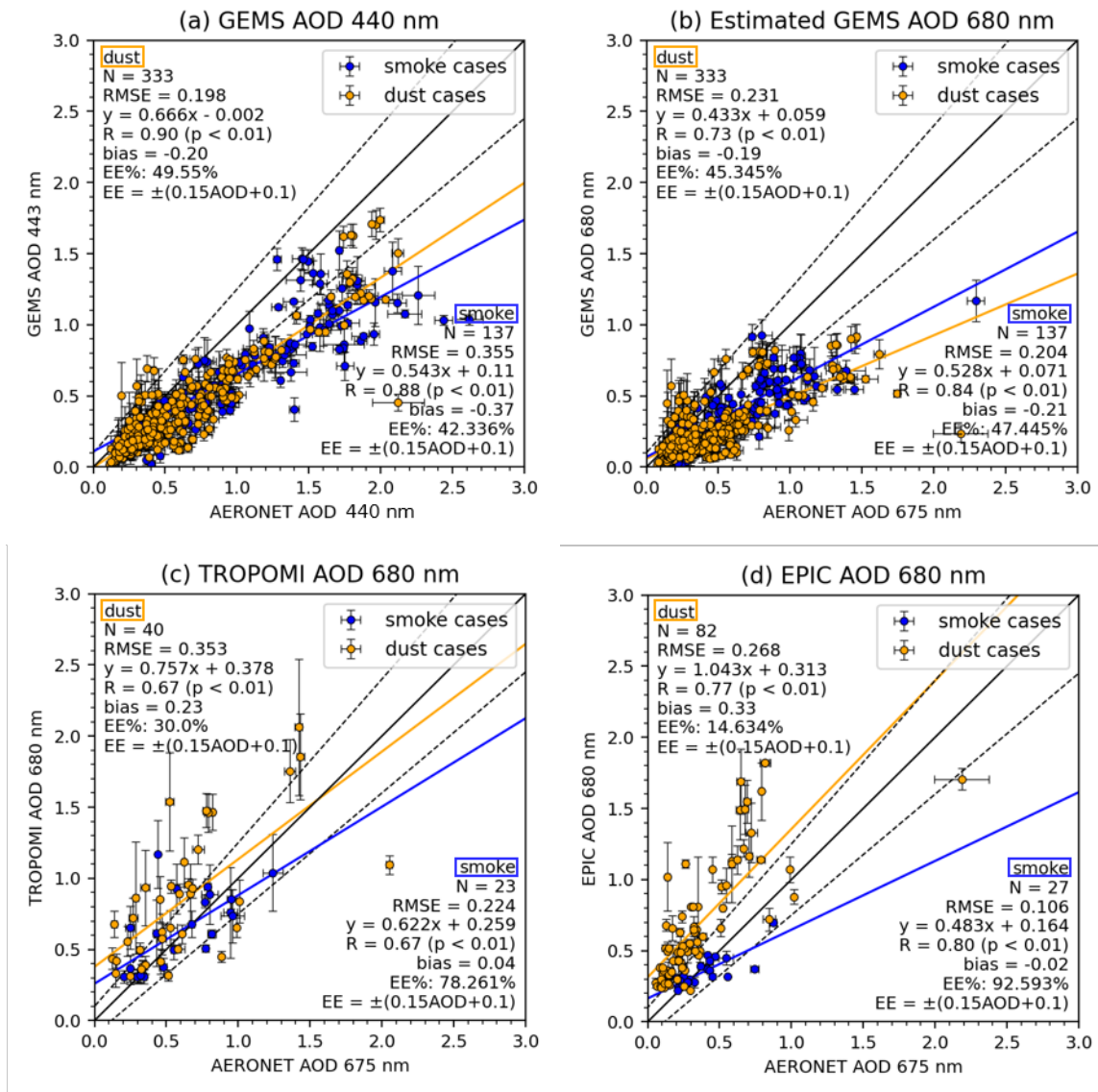
For all the dust and smoke cases listed in Table 1, the AOD products from GEMS, TROPOMI, and EPIC are first validated against the ground-based AERONET AOD data. Subsequently, a pixel-by-pixel intercomparison is conducted among the satellite products. Additionally, the ALH products from the three passive satellite measurements undergo validation using CALIOP level 2 aerosol extinction profile. These validated ALH products are then intercompared.

3.1 AOD intercomparison and validation with AERONET

The validation of the AOD products from GEMS, TROPOMI, and EPIC against AERONET AOD is shown in Fig. 3. GEMS AOD at 443 nm exhibits a strong positive correlation with AERONET AOD at 440 nm, with correlation coefficients (R) of 0.9 for dust cases and 0.88 for smoke cases (Fig. 3a). The validation results for GEMS AOD at 680 nm for smoke cases indicate a similar statistical agreement (R = 0.84) with 443 nm. In contrast, for dust cases at 680 nm compared with 443 nm, there are notable differences with decreased correlation coefficient (R = 0.73) and a 20 % decrease of RMSE. This indicates possible inaccuracies in the GEMS dust aerosol model but confirms the reliability of the smoke model. GEMS AOD at 680 nm show stronger underestimation than 443 nm, particularly noticeable when AERONET AOD exceeds 0.5. Furthermore, the bias increases with higher AOD levels, as shown in Fig. S1. The observed underestimation of GEMS AOD at 680 nm can be in part due to an overestimation of the Angstrom Exponent (AE), which can be affected from inaccurate particle size or refractive index in the wavelength-dependent aerosol model.

For dust cases, both TROPOMI and EPIC AOD show a positive bias compared to AERONET AOD, with values of 0.23 and 0.33 for TROPOMI and EPIC, respectively. Additionally, the comparison between EPIC and TROPOMI AOD with AERONET reveals a slope close to unity for dust cases (EPIC: 0.76, TROPOMI: 1.04), indicating the effectiveness of the dust aerosol model. In contrast to the dust cases, TROPOMI and EPIC AOD exhibit a negligible bias for smoke cases. Furthermore, the lower slope observed in the comparison for smoke cases (EPIC: 0.48, TROPOMI: 0.62) suggests that the smoke aerosol model is not as accurate as the dust aerosol model. The positive y-intercept observed for both EPIC and TROPOMI suggests that the surface reflectance employed in the dust aerosol model may be underestimated, resulting in an overestimation in AOD

retrieval. For TROPOMI and EPIC retrievals over land, climatological surface reflectance data from MODIS is employed. Additionally, unlike GEMS AEH retrieval algorithm that uses GEMS level 2 surface reflectance data, Cho et al. (2024) developed a new method for GEMS AOD retrieval, employing a novel hourly surface reflectance database generated through the minimum reflectance method, which integrates climatological minimum reflectance values for each pixel within a ± 15 -
 330 day window over a two-year period, along with monthly background AOD data. This novel surface reflectance estimation from GEMS AOD retrieval is shown effective. In summary, GEMS consistently underestimates AOD, especially at 680 nm, compared to AERONET AOD. EPIC and TROPOMI, while tending to overestimate AOD in dust cases due to underestimated surface reflectance, show a more accurate dust aerosol model than for smoke.



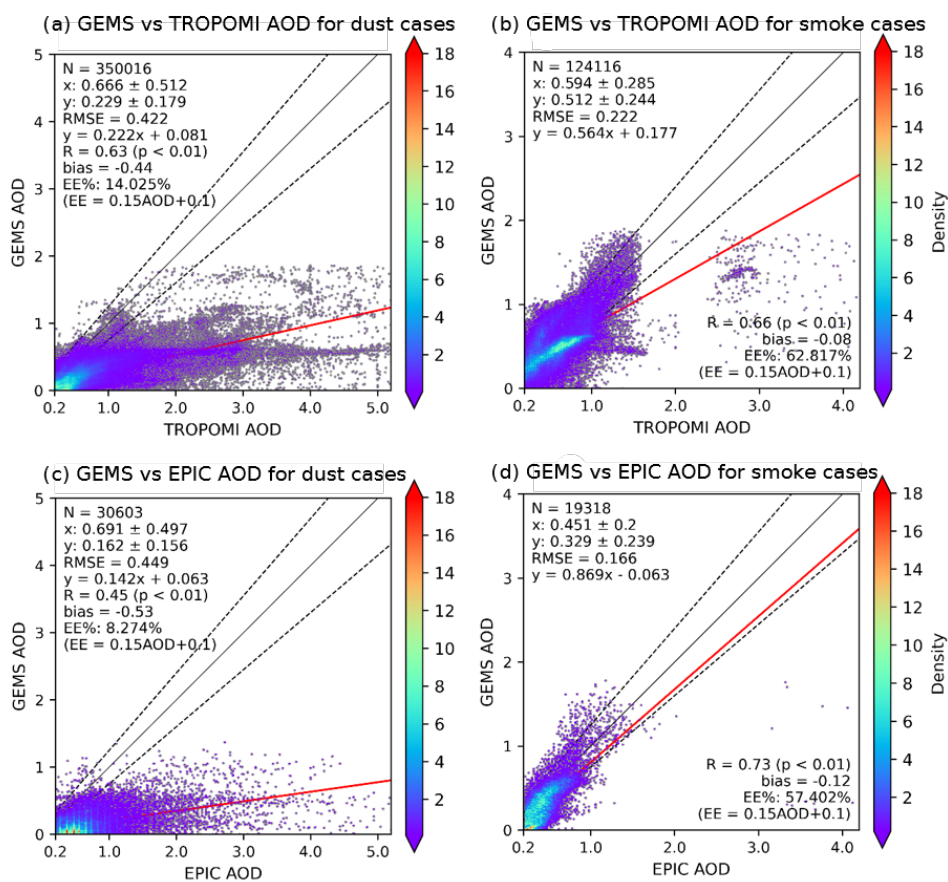
335 **Figure 3. Comparison of GEMS, TROPOMI, and EPIC AOD with AERONET AOD for all cases. The blue and yellow dots denote smoke and dust cases, respectively. (a) Comparison of GEMS AOD at 443 nm with AERONET AOD at 440 nm. (b) Comparison of estimated GEMS AOD at 680 nm, (c) TROPOMI AOD at 680 nm, and (d) EPIC AOD at 680 nm with AERONET AOD at 675 nm. The solid black line is the 1:1 line, the solid lines are the regression lines, and the dotted lines are error envelopes for AOD ($EE = \pm(0.15 AOD + 0.1)$). Annotated are the number of scatter points (N), root mean square error (RMSE), correlation coefficient (R), significance level (p), mean bias, and the percentage of data points within the error envelop (EE). Satellite data points only with a standard deviation less than 0.3 are shown for spatial consistency.**

340

Following the validation with AERONET AOD, Fig. 4 shows the comparison of GEMS AOD with TROPOMI and EPIC
 345 AOD, presented separately for dust and smoke cases. For dust cases, GEMS AOD is significantly lower compared with TROPOMI and EPIC, with negative mean biases of -0.44 and -0.53 for EPIC and TROPOMI, respectively. The inaccuracy of

the GEMS dust aerosol model, as identified in the previous AERONET validation (Fig. 3), have notable impact on the significant difference of GEMS AOD with TROPOMI and EPIC. Furthermore, surface reflectance issues observed in TROPOMI and EPIC further contribute to this disparity. Specifically, surface reflectance estimates for land surfaces from TROPOMI and EPIC may need refinement, as GEMS AOD values close to zero tend to be higher in TROPOMI and EPIC over land but not observed over water (Fig. S3). The smoke cases show a stronger agreement compared to dust cases, as indicated by decreased negative biases from -0.44 (-0.53) to -0.08 (-0.12) and RMSE values from 0.42 (0.45) to 0.24 (0.17) for TROPOMI (EPIC). The agreement is particularly robust between GEMS and EPIC, as indicated by a high R-value of 0.73. While the smoke aerosol model employed in TROPOMI and EPIC is not as effective as the dust model, its impact on the comparison is relatively minor. These factors on the aerosol model including aerosol properties, fine mode fraction, and the phase function, as well as the SSA, can largely influence the accuracy of AOD retrievals. Furthermore, AOD sensitivity on changing SSA and surface reflectance is shown in Fig. S4. A detailed table including the aerosol models employed in the AOD retrieval is provided in Table S1.

360



365 **Figure 4. GEMS AOD compared with the corresponding TROPOMI and EPIC products for dust and smoke cases. Scatter density plots of (a) GEMS AOD versus TROPOMI AOD for dust cases, (b) same as (a) but for smoke cases, (c) GEMS AOD versus EPIC AOD for dust cases, and (d) same as (c) but for smoke cases. Black solid line is the one-to-one line, and the red solid line is the regression line. The dotted lines on the AOD comparison plots (a), (c), indicates error envelopes ($EE = \pm 0.15 AOD + 0.1$). TROPOMI and EPIC AOD does not have retrieval for less than 0.2, therefore, the figures axis start from where the data exists.**

3.2 UVAI intercomparison

370 The UVAI products of the three satellites are compared, since UVAI is used as a criterion to focus on retrieving absorbing aerosols for the current TROPOMI and EPIC AOD retrievals. Figure 5 compares GEMS UVAI with TROPOMI UVAI (Fig. 5a) and EPIC UVAI (Fig. 5b) for all cases. Compared with TROPOMI, GEMS UVAI is systematically higher with a positive

mean difference of 1.21. Compared with EPIC, GEMS also exhibits a positive bias, although to a lesser extent (0.32), and shows a higher correlation ($R = 0.57$). This suggests that when employing UVAI as a filtering criterion for identifying absorbing aerosols in the EPIC and TROPOMI AOCCH retrievals, it is important to establish a threshold that takes into account the differences among these distinct products. The differences in the GEMS, TROPOMI, and EPIC UVAI products can be caused by several reasons. First, different wavelengths are used to derive the UVAI product: GEMS UVAI is derived from radiances at 354 nm and 388 nm, whereas TROPOMI and EPIC UVAs are derived from radiances at 340 nm and 380 nm. Additionally, pressure assumption and resolution differences can cause the differences of their UVAI retrievals. We included EPIC and TROPOMI UVAI comparison scatter plot in Fig. S5. To summarize, GEMS UVAI is systematically higher than TROPOMI and is more comparable to EPIC.

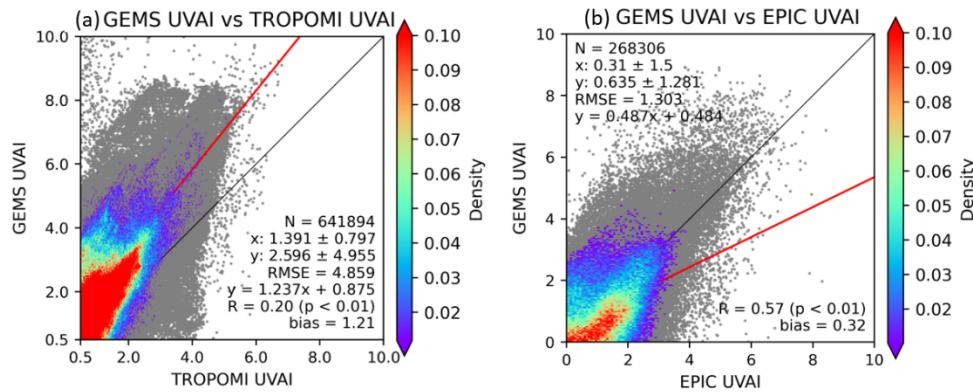


Figure 5. Comparison of GEMS UVAI with corresponding TROPOMI and EPIC products. Scatter density plots illustrating (a) GEMS UVAI vs. TROPOMI UVAI and (b) GEMS UVAI vs. EPIC UVAI. The one-to-one line is represented by a black solid line, while the regression line is shown in red. Dust and smoke cases are combined due to their similarity. Note that TROPOMI UVAI does not include retrieval values below 0.5, thus the axis begins at a minimum value of 0.5.

3.3 ALH validation with CALIOP

To ensure the comparison of the same variable, it is critical to account for differences arising from different ALH definitions as detailed in Section 2.2. As such, the ALH values of all passive sensors are converted to AOCCH following the CALIOP AOCCH definition when validated by CALIOP data. The comparison between the derived AOCCH for the three passive sensors and the CALIOP AOCCH is depicted in Fig. 6. Both EPIC and TROPOMI show higher AOCCH values compared to CALIOP, with a bias of 0.8 km for both sensors. Additionally, the RMSE for EPIC and TROPOMI are 1.25 km and 1.31 km, respectively. In contrast, GEMS shows a minimal bias, accompanied by a lower RMSE of 0.75. Despite the overestimation observed in EPIC and TROPOMI, their correlation with CALIOP is notably high ($R=0.75$ and $R=0.71$ respectively), while GEMS exhibits a slightly lower correlation ($R=0.64$). The major contribution to the overestimations observed in EPIC and TROPOMI come from the smoke cases over Southeast Asia (B4, B5, and B6). This suggests a potential issue with the smoke aerosol model in the EPIC and TROPOMI AOCCH algorithms when applied over Southeast Asia, which warrants further investigation. Furthermore, AOCCH sensitivity on changing surface reflectance and SSA is shown in Fig. S4.

GEMS AEH algorithm retrieves both absorbing and non-absorbing aerosols, resulting in a larger dataset available for comparison. In contrast, EPIC and TROPOMI exclusively retrieve AOCCH for absorbing aerosols, which are determined based on UVAI (e.g., $UVAI > 1$ for TROPOMI and $UVAI > 1.5$ for EPIC). It is therefore desirable to assess the GEMS AEH retrieval accuracy under different aerosol characteristics. We categorize GEMS aerosol retrievals into two groups using a GEMS UVAI threshold of 3 ($UVAI < 3$ and $UVAI \geq 3$) in the subsequent analyses (Fig. 6c-d). The overall agreement between GEMS and

CALIOP is better for aerosols with UVAI ≥ 3 than those with UVAI < 3 , particularly for dust cases, as evidenced by a higher R-value (0.75 compared to 0.42) and a lower RMSE (0.33 compared to 0.89). The improved performance for UVAI ≥ 3 can be attributed to the stronger signals of aerosol layers detected in the O₂-O₂ absorption band. Furthermore, as observed in Fig. 6b, the mean bias of AOCHE tends to be higher at 0.2 in smoke cases compared to -0.01 in dust cases.

Table 2. Comparison of GEMS, TROPOMI, and EPIC AOCHE with CALIOP AOCHE measurements in Figure 6a.

	N	EE (km)	RMSE (km)	Regression equation	x	y	R
GEMS	643	± 0.7	0.75	$y = 0.614x + 0.918$	2.1 ± 0.9	2.2 ± 0.9	0.64
EPIC	165	± 1.2	1.25	$y = 1.025x + 0.749$	2.5 ± 1.1	3.3 ± 1.4	0.75
TROPOMI	144	± 1.2	1.3	$y = 1.111x + 0.510$	2.4 ± 1.0	3.2 ± 1.5	0.71

415

Table 3. Comparison of GEMS with CALIOP AOCHE for dust and smoke cases in Figure 6b-d.

	Dust cases					Smoke cases				
	N	R	RMSE (km)	Bias (km)	Regression equation	N	R	RMSE (km)	Bias (km)	Regression equation
All	267	0.46	0.771	0	$y = 0.684x + 0.63$	376	0.52	0.707	0.2	$y = 0.293x + 1.949$
UVAI < 3	193	0.42	0.884	-0.01	$y = 0.562x + 0.684$	308	0.55	0.656	0.34	$y = 0.315x + 1.931$
UVAI ≥ 3	74	0.75	0.328	0.03	$y = 0.636x + 0.511$	68	0.57	0.542	-0.46	$y = 0.468x + 1.239$

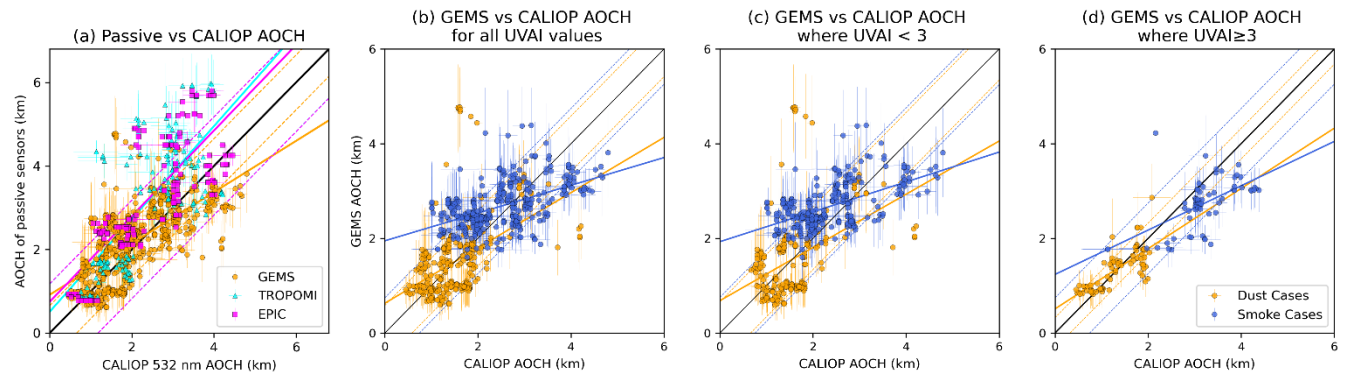


Figure 6. Comparison of GEMS, TROPOMI, and EPIC AOCHE with CALIOP measurements for all cases. (a) Scatterplot of GEMS (orange), TROPOMI (cyan), and EPIC (magenta) AOCHE versus CALIOP AOCHE. The black solid line indicates one-to-one line and the dotted lines represent error envelop within which one standard deviation data points are for each passive satellite product. Panels (b) – (d) are scatter plots of GEMS versus CALIOP AOCHE: (b) is for all data points, (c) is AOCHE where GEMS UVAI < 3 , and (d) is for AOCHE where GEMS UVAI ≥ 3 . For (b) – (d), orange dots indicate data points for dust cases and blue dots for smoke cases.

Based on a 2% measurement uncertainty for the EPIC DOAS ratios Geogdzhayev and Marshak (2018), the theoretical AOCHE retrieval error is shown to remain below 1.25 km for vegetated surface when AOCHE exceeds 1 km (Xu et al., 2019). Our analysis shows that the RMSE from all error sources, including measurement and retrieval uncertainties, evaluated between EPIC and CALIOP is approximately 1.25 km, which aligns with the retrieval error. The TROPOMI AOCHE algorithm builds upon the framework established by the EPIC algorithm (Xu et al., 2019), with some adjustments for TROPOMI. Measurement uncertainty for TROPOMI is estimated to be 1 – 2 % (Kleipool et al., 2018). In addition to instrument errors, TROPOMI

AOCH algorithm incorporates the convolution of TROPOMI spectral data, introducing potential additional uncertainty. Our study indicates an RMSE of 1.31 km for all error sources for TROPOMI AOCHE. Assuming retrieval error similar to EPIC, this uncertainty appears reasonable. The GEMS AEH algorithm originates from Park et al. (2016), who performed an error analysis for OMI. The instrument error was indicated to be less than 10 m, stemming from a spectral wavelength error of 0.02 nm, with the total error ranging from 739 to 1276 m depending on aerosol types. Meanwhile GEMS has a spectral calibration accuracy of 0.002 nm (Kang et al., 2020). Our study demonstrates an RMSE of GEMS ALH at 0.75 km, falling within the theoretical retrieval error.

440

3.4 Passive ALH inter-comparison

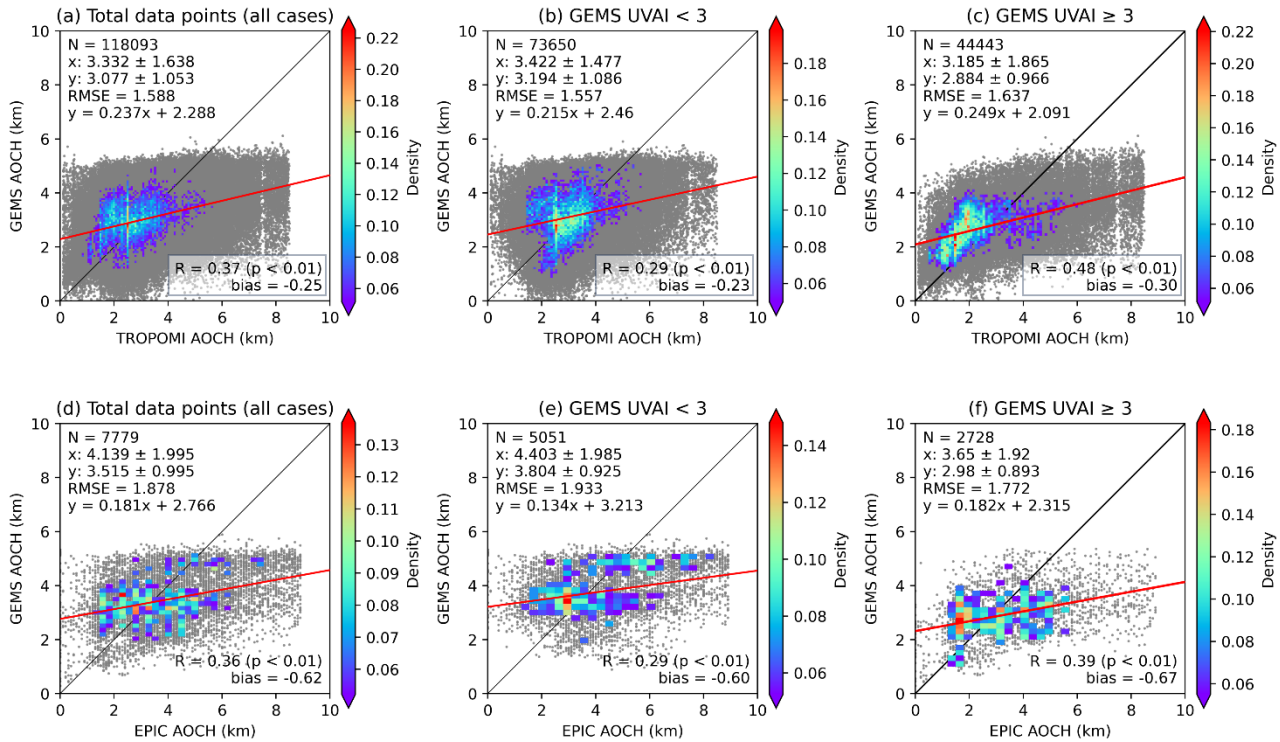
Upon resampling GEMS products to match the spatial resolution of TROPOMI and EPIC, we synchronize the observation times through linear interpolation of the hourly GEMS products to facilitate a pixel-by-pixel comparison for all ALH products. To address the possible discrepancies stemming from different ALH definitions mentioned in Section 2.2, GEMS AEH is converted to align with the EPIC and TROPOMI AOCHE definition. Furthermore, we categorize GEMS aerosol retrievals into two groups ($UVAI < 3$ and $UVAI \geq 3$), similar to the analyses in Section 3.3.

The results of the ALH inter-comparison for both dust and smoke cases are given in Fig. 7. GEMS AOCHE exhibits a narrower range compared to TROPOMI and EPIC, which can be attributed to the different range limits used in their algorithm lookup table (LUT). GEMS only allows AEH to vary within the range from 0.2 to 5 km (Park et al., 2023), while EPIC and TROPOMI AOCHE ranges from 0 to 9 km. Moreover, GEMS exhibits a negative mean difference of -0.25 and -0.62 when compared to EPIC and TROPOMI AOCHE, observed across all dust and smoke cases, and across both UVAI classifications. It is observed that aerosols with $UVAI \geq 3$ exhibit a stronger correlation with GEMS AOCHE compared with aerosols with $UVAI < 3$. This can be attributed to the O_2 or O_2-O_2 absorption band being more sensitive to aerosols with higher UVAI values. Setting the UVAI threshold to 4 enhances the statistical performance for $UVAI \geq 4$, with an increase in correlation coefficients from 0.48 to 0.61 for TROPOMI and 0.39 to 0.46 for EPIC (Fig. S6).

Although our study cases show no CALIOP AOCHE values above 5 km (Fig.6), TROPOMI and EPIC AOCHE retrievals indicate values exceeding this altitude. This is a combination of inaccurate cloud detection and inherent sensitivity in the retrieval process. While some areas are influenced by cloud contamination, most of the high AOCHE areas tend to have low AOD and not being influenced by clouds (Fig. S8 & S10). Since AOCHE is more sensitive to higher AOD (Xu et al., 2017), there is greater uncertainty in AOCHE retrievals in regions with lower AOD. Furthermore, these high AOCHE areas do not show high UVAI values greater than 4; instead, they exhibit values around 1-2, using GEMS UVAI as a reference. Therefore, both cloud

460

detection inaccuracies and the low sensitivity of Aoch retrieval to low AOD contribute to the observed high Aoch in these areas, with the latter being more dominant in our selected cases.



465 **Figure 7. Intercomparison of GEMS, TROPOMI and EPIC Aoch for dust and smoke cases as a function of UVAI. Density scatter plot of (a) GEMS and TROPOMI Aoch comparison and (d) GEMS and EPIC Aoch comparison for all dust cases. (b) and (c) are same as (a) but for GEMS UVAI < 3 and UVAI ≥ 3, respectively. (e) and (f) are same as (d) but for GEMS UVAI < 3 and UVAI ≥ 3, respectively. GEMS AEH converted into EPIC (or TROPOMI) Aoch definition.**

470 3.5 Diurnal variation of GEMS and EPIC ALH

We present a comparison of the diurnal variations of ALH in GEMS hourly observations with close-hourly EPIC measurements, which provide between two to six daily observations within our region of interest. Our study domain encompasses a wide geographical area, with selected cases spanning from March to August, introducing seasonal changes that result in significant shifts in the sun's position. Therefore, we define the relative local solar noon time for a given day as the point when the solar zenith angle at a particular location reaches its minimum value. Using this relative local solar noon time as the central reference point, GEMS and EPIC products for the day are adjusted to relative local solar time (LST) accordingly. Additionally, GEMS AEH was converted into the Aoch definition. Figure 8 illustrates the hourly diurnal variations of both GEMS and EPIC Aoch.

The diurnal pattern of EPIC Aoch values reveals a notable ascent in the morning, starting from heights below 3 km around 7-8 LST, peaking at approximately 4.5 km during 11-12 LST, followed by a marginal decline to approximately 3.5 km at 14-15 LST. Conversely, GEMS Aoch remains relatively stable (around 4 km) until a more pronounced descent occurs after 10 LST, reaching less than 3 km at 14-15 LST. Note that most of the time, GEMS Aoch values are lower compared to EPIC. The diurnal variation of Aoch reveals a slightly different pattern when UVAI exceeds 3 (Fig. 8b). GEMS Aoch when UVAI > 3 shows a gradual increase until around 10-11 LST, followed by a notable decline, consistently maintaining lower Aoch values compared to the dataset inclusive of all UVAI values. Conversely, EPIC Aoch remains relatively steady until experiencing a rise between 10-14 LST, subsequently declining at 14-15 LST. There are notable differences in Aoch

diurnal variation between GEMS and EPIC, with GEMS showing a significant decrease throughout the daytime, whereas EPIC exhibits a gradual increase followed by a subsequent drop.

Previous studies indicate that ALH tends to be higher in the afternoon, a phenomenon that may be partially affected by the PBLH. Xu et al. (2017) found higher EPIC AOCHE in the afternoon, possibly indicating a relationship with the diurnal evolution of tropospheric convection. Lee et al. (2019) observed that aerosol heights tend to rise in the afternoon and early evening, likely due to the development of the boundary layer's mixed layer. Lu et al. (2023) conjecture that the diurnal cycle (rising in the morning and descending in the afternoon) of Saharan dust plume height is a consequence of the diurnal variation in solar heating, which leads to thermal buoyancy lifting the dust layer, combined with the diurnal evolution of the boundary layer. Unfortunately, our dataset lacks sufficient information beyond 15 LST, making it challenging to discern the relationship between AOCHE and PBLH, particularly when the PBL collapses in the late afternoon. Therefore, we examined three years of Modern-Era Retrospective Analysis for Research and Applications, Version 2 (MERRA-2) data from 2021 to 2023, focusing on March within the East Asia domain. MERRA-2 AOCHE is defined same as the CALIOP AOCHE in the manuscript, weighted by optical depth at each vertical layer using aerosol extinction vertical profiles. A similar diurnal variation is observed between the PBLH and MERRA-2 AOCHE calculated with the aerosol extinction below the PBLH (Fig. S7). This indicates that when most aerosols locate within the PBL, diurnal variation is affected by the PBL process, which changes the PBLH during daytime. The diurnal variation of EPIC AOCHE from Fig. 8 is consistent with the MERRA-2 PBLH and AOCHE calculated by extinction below the PBL, as ascending throughout the morning and descending after 2 pm local time, although EPIC AOCHE values are higher than MERRA-2 AOCHE, due to its constraint by PBLH. The diurnal variation of GEMS and MERRA-2 AOCHE show similarities for the afternoon decrease. However, GEMS AOCHE, which shows an overall decrease throughout the day, does not coincide with the MERRA-2 data, which shows an increase until 14 local time. Despite the comparison of ALH diurnal variation from satellite observations and model reanalysis, the validation of the diurnal variation of ALH still remains a significant challenge due to a lack of spatially and temporally resolved active remote sensing measurements. In addition, for passive remote sensing, potential artifacts such as scattering angle bias for geostationary satellites and contamination of cloud edges may influence the diurnal cycle of aerosol height. Additionally, the limited data points obtained from selected case study dates could introduce uncertainty when attempting to generalize the ALH diurnal cycle.

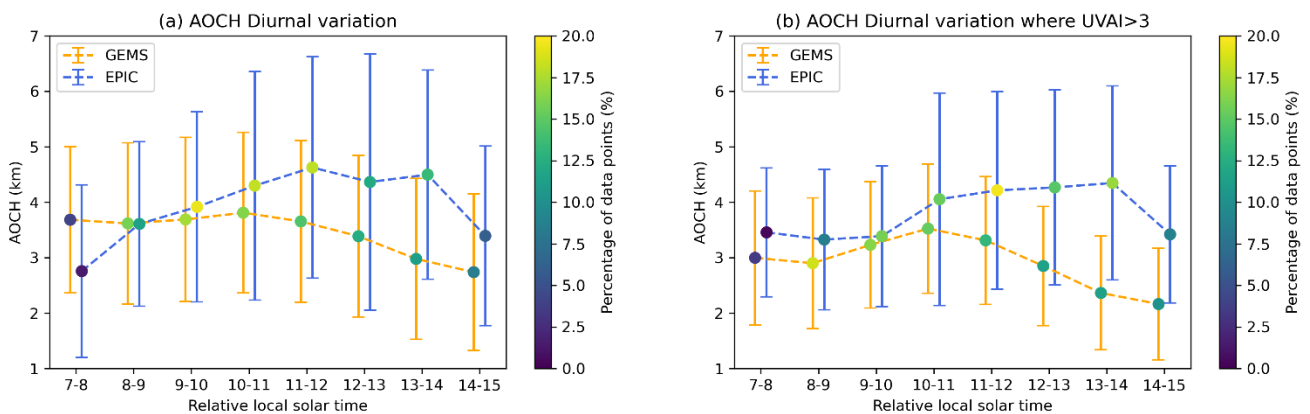


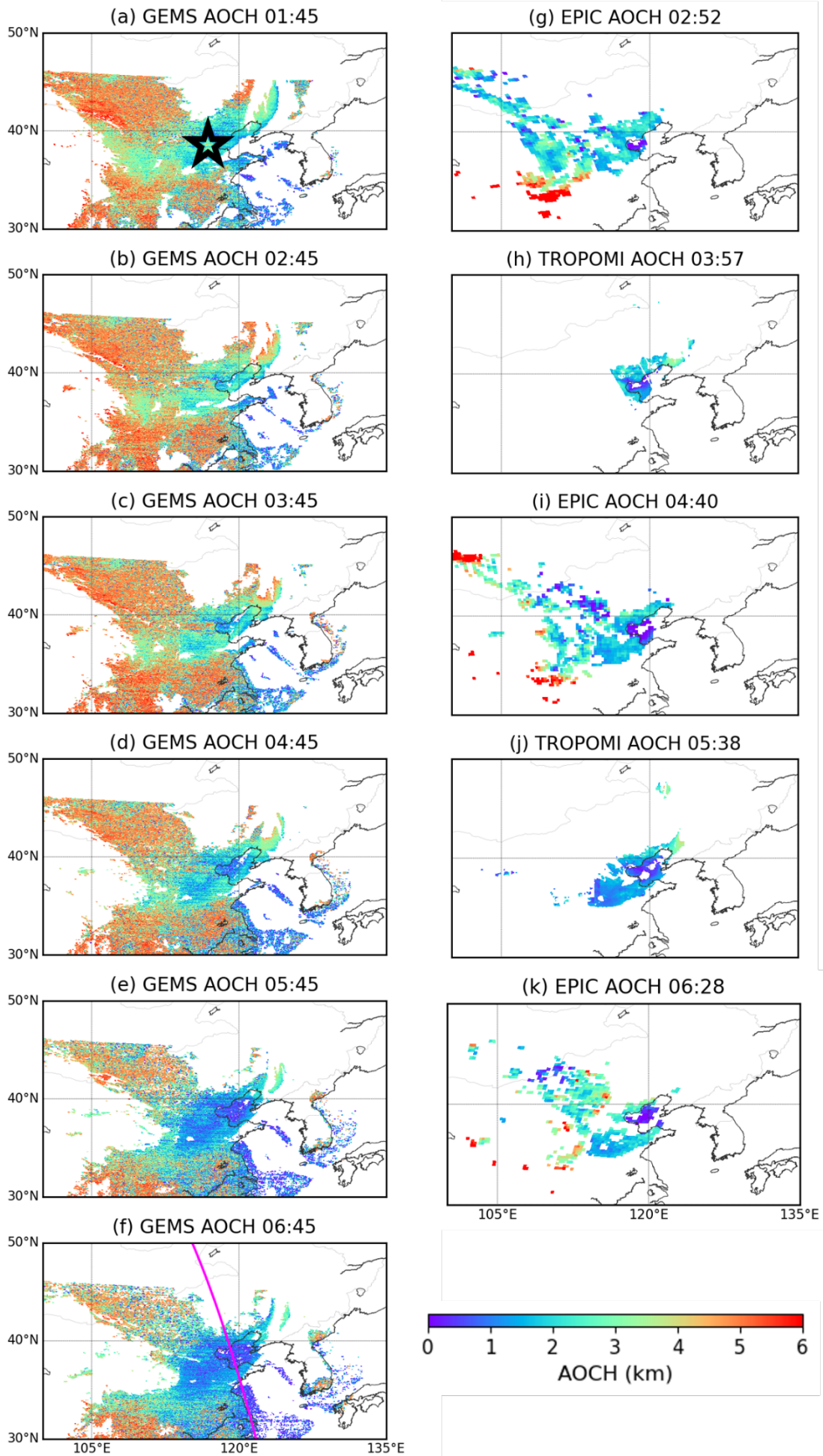
Figure 8. Diurnal variation of AOCHE between GEMS and EPIC at relative local solar times. (a) AOCHE diurnal variation for all pixels, (a) same as (a), but only for UVAI > 3. Yellow lines indicate GEMS AOCHE error bar (standard deviation), blue indicates the corresponding of EPIC AOCHE, dots represent the percentage of data points during each hour. GEMS AEH has been adjusted to match the EPIC AOCHE definition.

4 Case study

We present detailed analysis of GEMS, EPIC, and TROPOMI ALH retrievals during transport for a dust (D1) and a smoke
520 plume (B6). Diurnal variations of ALH from GEMS and EPIC for the dust or smoke cases are also discussed.

4.1 Dust plume case

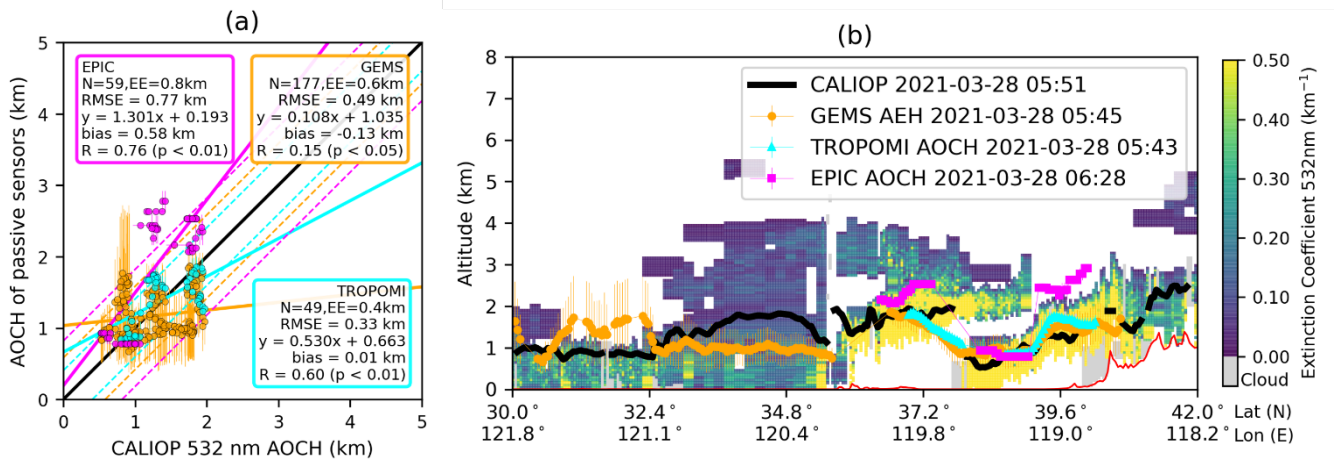
Figure 9 shows GEMS, TROPOMI and EPIC ALH retrievals for a selected dust case on March 28, 2021 (D1). GEMS AEH
was adjusted to EPIC/TROPOMI AOC definition for consistent comparison. The first row presents GEMS AOC, with
525 magenta lines depicting CALIOP ground track over the GEMS map at the closest time of CALIOP measurement and the
second row shows EPIC and TROPOMI AOC aligned with the closest GEMS measurement time. The AOD, UVAI maps
for all satellites are shown in the Fig. S8. This case is a spring dust event, originating from the Gobi Desert a few days before
it reached over China on 28 March 2021, specifically near Beijing, indicated by the black star on the middle of the research
domain (Fig. 9a). In the dust plume area, GEMS AOC peaks at high values (~3 km) at 01:45 and 02:45 (Fig. 9a-b) before
gradually decreasing to ~1.5 km by 06:45 (Fig. 9f). In contrast, EPIC and TROPOMI AOC maintain a relatively consistent
530 values at 1-2 km. Likely, hourly GEMS observations reveal clear hourly variations, whereas discerning diurnal changes is
challenging with TROPOMI and EPIC.



535 **Figure 9.** The first column (a – f) shows hourly GEMS AOC (GEMS AEH adjusted to EPIC/TROPOMI AOC definition) from (a) 01:45 to (f) 06:45 (UTC). Second column (g – k) EPIC and TROPOMI AOC aligned with the nearest GEMS observation times for a dust plume event on 28 March 2021. The magenta line on the GEMS maps in the first column indicates the CALIOP ground tracks, which have the closest observation times with GEMS.

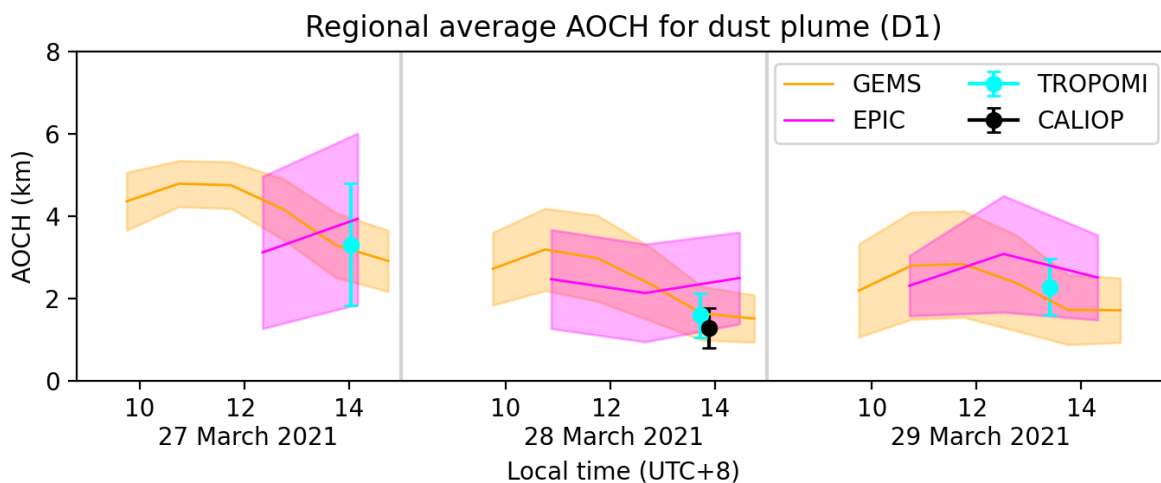
After converting all passive ALH products to the CALIOP AOC definition, the comparison of GEMS, TROPOMI, and EPIC
 540 AOC with CALIOP AOC for this dust case was conducted and is shown in Fig. 10. GEMS has the greatest number of data points due to its valid retrievals for both scattering and absorbing aerosols and its high spatial resolution. For this specific case, EPIC AOC show the highest correlation coefficient among all ($R = 0.74$) and TROPOMI AOC also has a high correlation coefficient ($R = 0.6$) and the lowest RMSE of 0.33 km. Although CALIOP can capture multiple layers of aerosols from extinction coefficients, passive sensors used in this study assume single vertical profile, thereby retrieving AOC where
 545 stronger signal is detected. In Fig. 10b, CALIOP identifies discontinuous high extinction coefficients at 38° N latitude and 119.5° E longitude leading to a discontinuous CALIOP AOC. While EPIC AOC shows the discontinuity from the absence of the retrieval in between the two layers, GEMS and TROPOMI exhibit continuous retrievals, consistently following the stronger signal. Consequently, discrepancies between CALIOP and passive sensors may be more pronounced in the presence of multiple aerosol layers. Further investigation is needed for a comprehensive study of multi-layered aerosol plumes.

550



555 **Figure 10.** Comparison of GEMS, TROPOMI and EPIC AOC with CALIOP AOC for a dust case over East Asia on 28 March 2021. (a) GEMS, TROPOMI, and EPIC AOC on the vertical profile of CALIOP aerosol extinction curtain plot. (b) Scatterplot of GEMS (orange), TROPOMI (cyan), and EPIC (magenta) versus CALIOP AOC definition.

Figure 11 shows the regional averaged ALH during this dust plume transport from 27 to 29 March 2021. To focus on the consistent area covered by the thickest dust plume, different UVAI thresholds were empirically selected. Pixels where UVAI values of their own products are higher than 3, 1, and 2 were considered for GEMS, TROPOMI, and EPIC, respectively. For
 560 CALIOP, collocated pixels along the track with GEMS UVAI > 3 were considered. Maps of regional ALH and UVAI for all products are provided in Fig. S9. The mean AOC values of the dust plume from all products show good agreement, falling within reasonable error range of < 1 km. From GEMS measurements, the dust plume locates at 4-5 km on 27th March, then descends to ~3 km during 28th March and keeps until 29th, similar as EPIC and TROPOMI measurements, indicating the deposition process of dust aerosols during transport. Although daily mean of the AOC values change during the plume
 565 transport, GEMS show similar diurnal variation each day, increase in early morning followed by a consistent decrease throughout the daytime.

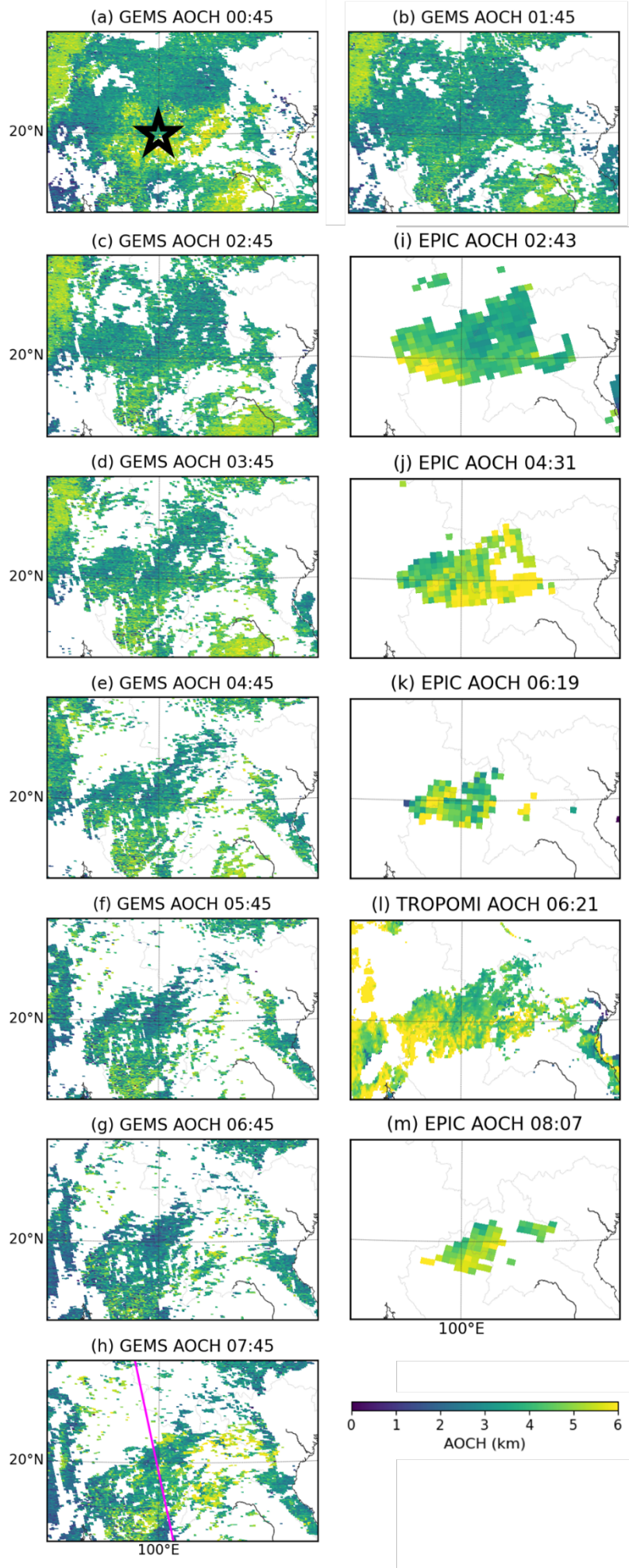


570 **Figure 11. Time series plot of regional average AOCHE for a dust plume on 28 March 2021 (D1). AOCHE of GEMS, TROPOMI, and EPIC is represented as orange, cyan, and magenta, respectively. The lines and shadows indicate the mean and the standard deviation, respectively. CALIOP AOCHE is represented by the black error bar. GEMS AEH, EPIC AOCHE, and TROPOMI AOCHE are all converted to the CALIOP AOCHE definition.**

4.2 Smoke plume case

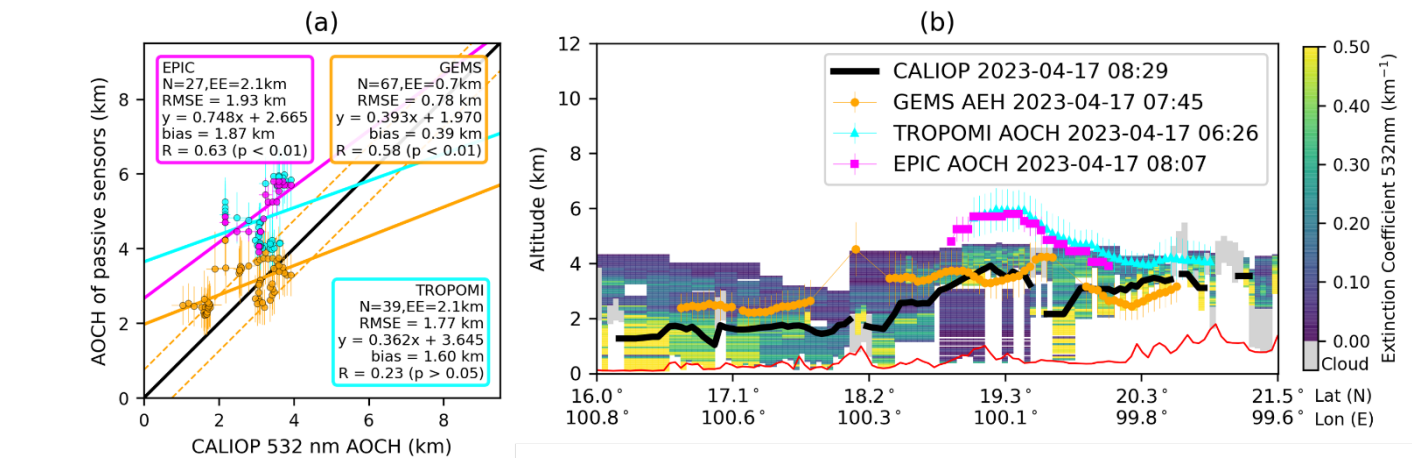
575 Figure 12 displays ALH retrievals from GEMS with TROPOMI and EPIC for one of the selected smoke case on April 17, 2023 (B6). The first row displays GEMS AOCHE, converted from GEMS AEH to match the EPIC/TROPOMI AOCHE definition. The second row shows EPIC and TROPOMI AOCHE aligned with the closest GEMS measurement time. In addition, AOD and UVAI maps are provided in Fig. S10. This particular case is a smoke event in Southeast Asia, with the identified smoke plume situated predominantly over the northern areas of Laos and Thailand, shown in the central part of the domain (20° N, 100° E) indicated by the black star on Fig. 12a. Over the previous decades, the air quality in Southeast Asia has been periodically affected by the transboundary smoke and haze issue, primarily linked to slash-and-burn agriculture and land clearing practices, particularly during the dry season (Shi et al., 2014; Chang and Song, 2010). Focusing on the smoke plume that can be identified from EPIC/TROPOMI AOCHE retrieval for absorbing aerosols, GEMS AOCHE ranges from 3 to 5 km, while EPIC and TROPOMI consistently show values predominantly exceeding 4 km over land. The decrease in EPIC AOCHE spatial coverage throughout the day, coupled with an increase in AOCHE values (Fig 12i & j), indicates the dissipation process of the smoke plume.

585



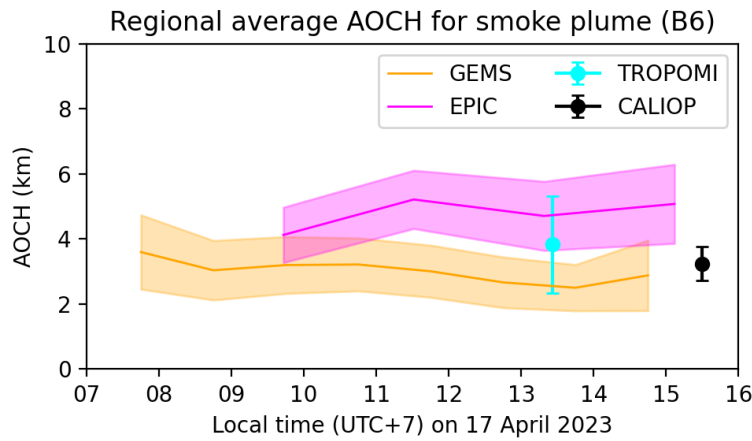
590 **Figure 12.** The first row (a – f) shows hourly GEMS AOC (GEMS AEH adjusted to EPIC/TROPOMI AOC definition) from (a) 00:45 to (f) 07:45 (UTC). Second row (g – i) EPIC and TROPOMI AOC aligned on the nearest GEMS measurement times for a smoke plume event on 17 April 2023. The magenta line on the GEMS maps in the first column indicates the CALIOP ground tracks, which have the closest observation times with GEMS.

Figure 13 presents a comparison with CALIOP AOC, specifically highlighting the northern regions of Laos and Thailand where the smoke plume is detected along the CALIOP ground track. GEMS AEH and EPIC/TROPOMI AOC values have been converted to the CALIOP AOC definition. GEMS and CALIOP AOC show comparability within the range of 2-4 km, as evidenced by a smaller RMSE of 0.75 km. On the contrary, EPIC and TROPOMI ALH values are approximately 2 km higher than CALIOP ALH, yet they display similar vertical distribution patterns of the smoke plume over the region of 19-20° N. This suggests that EPIC and TROPOMI AOC retrievals exhibit a systematic positive bias for aerosols over Southeast Asia, indicating the potential need for tuning in the related smoke model, including surface reflectance and aerosol properties like size distribution, refractive index, single scattering albedo. In general, GEMS demonstrates comparability with CALIOP AOC, whereas both EPIC and TROPOMI ALH tend to overestimate.



605 **Figure 13.** Same as Figure 11 but for a smoke case over Southeast Asia on 17 April 2023.

In Fig. 14, we present the regional averaged ALH for absorbing aerosols for this smoke case. UVAI thresholds are chosen to facilitate the comparison of ALH among GEMS, EPIC, and TROPOMI, ensuring a consistent focus on regions with comparable coverage of absorbing aerosols. UVAI thresholds for GEMS, TROPOMI, and EPIC, are set as 3, 1.5, and 2, respectively. Detailed regional ALH map from all products are provided in Fig. S11. Notably, since the CALIOP product is included, all GEMS AEH and EPIC/TROPOMI AOC values have been converted to the CALIOP AOC definition. In contrast to the dust case discussed in Section 4.1, this smoke plume shows little diurnal variation throughout the day according to GEMS, and an overall slight increase observed by EPIC. Post 5 UTC time, GEMS and EPIC exhibit similar patterns, yet EPIC consistently registers ALH values approximately 2 km higher throughout the day. While the observation times of CALIOP do not align with the consecutive data of GEMS, the regional average of CALIOP AOC falls within the range of GEMS AOC. Additionally, the regional mean of TROPOMI AOC is higher than that of GEMS but lower than EPIC for this smoke plume.



620

Figure 14. Time series plot of regional average AOCHE for a smoke plume on 17 April 2023. AOCHE of GEMS, TROPOMI, and EPIC is represented as orange, cyan, and magenta, respectively. The lines and shadows indicate the mean and the standard deviation, respectively. CALIOP AOCHE is represented by the black error bar. GEMS AEH, EPIC AOCHE, and TROPOMI AOCHE are all converted to CALIOP AOCHE definition.

625

5 Conclusion and discussion

Aerosol vertical distribution is important for assessing aerosol climate impact, surface air quality, and remote sensing of aerosols. In this study, we compared multiple aerosol layer height (ALH) products from satellite platforms of GEMS, EPIC, and TROPOMI that use oxygen (or oxygen dimer) absorption bands, specifically O_2-O_2 band for GEMS, and O_2 A and B bands for TROPOMI and EPIC. Several dust and smoke plume cases over different regions in Asia covered by the field of regard of GEMS were selected for comparison. Adjustments have been made to account for the inherent variations in the definitions of ALH among different products, ensuring an apple-to-apple comparison.

As part of the ALH retrieval evaluation, we also evaluated the AOD retrievals from GEMS, EPIC and TROPOMI with AERONET AOD and compared the UVAI among these satellite platforms. Compared with AERONET, GEMS AOD at 443 nm demonstrates a strong positive correlation in both dust ($R = 0.9$) and smoke cases ($R = 0.88$). Discrepancies arise at 680 nm for dust cases, indicating potential inaccuracies in GEMS dust aerosol model. TROPOMI and EPIC tend to overestimate AOD in dust cases due to underestimated surface reflectance. The inaccuracies in the GEMS dust aerosol model significantly contribute to the substantial differences in GEMS AOD compared to TROPOMI and EPIC, further compounded by inaccurate surface reflectance in TROPOMI and EPIC. In addition, GEMS UVAI is consistently larger than TROPOMI UVAI, by 1.2, whereas it shows a better agreement with EPIC UVAI with a smaller bias of 0.32.

Both EPIC and TROPOMI consistently overestimates ALH in comparison to CALIOP, with an approximate bias of 0.8 km. In contrast, GEMS ALH demonstrated minimal bias but exhibited a slightly lower correlation coefficient ($R = 0.64$). Categorizing GEMS aerosol retrievals based on a UVAI threshold of 3 revealed better overall agreement with CALIOP ALH for aerosols with $UVAI \geq 3$. While comparing GEMS with EPIC and TROPOMI, a narrower range in GEMS AEH was seen due in part to limitations in its algorithm lookup table (LUT) within the range of 0.2 to 5 km, while EPIC and TROPOMI had LUTs extending from 0 to 9 km.

The diurnal pattern of EPIC AOCHE values shows a morning ascent and declining after noon, while GEMS remains relatively stable until a more pronounced descent in the late morning and early afternoon. MERRA-2 data analysis indicates a similar diurnal variation between PBLH and MERRA-2 AOCHE, suggesting that when most aerosols are within the PBL, their diurnal

variation is affected by the PBL process. The validation of the diurnal variation of ALH is very challenging due to limited spatial and temporal resolution in active remote sensing measurements and potential artifacts in passive remote sensing data.

655

Lastly, we presented a detailed analysis on both a dust case and a smoke case to compare differences in spatial and vertical distribution of ALH products, along with diurnal variations. EPIC and TROPOMI ALH show a strong correlation with CALIOP for both the discussed dust and smoke events; however, they tend to overestimate in the smoke case. In contrast, while GEMS ALH has a lower correlation, it consistently shows a smaller mean bias. Additionally, hourly GEMS ALH have the power to catch the diurnal variation of aerosol plumes during transport, compensating for the lack of measurements from other satellite platforms.

660

In conclusion, our comprehensive analysis provides a thorough evaluation of the performance and comparative assessment of ALH, AOD, and UVAI retrievals from GEMS, EPIC, and TROPOMI. The comparison of the ALH definition among different sensors highlights the need for standardization, ensuring a consistent basis for comparisons. Results from this study help enhance our understanding of aerosol plume characteristics, overcoming challenges associated with previously difficult aspects such as the comparison of ALH diurnal variations. Furthermore, we offer insights for future ALH product development by identifying and addressing the limitations in inputs from each retrieval algorithm, such as the impact of aerosol models and surface reflectance.

665

670

Appendix A: List of acronyms

AOD	Aerosol optical depth
SSA	Single scattering albedo
UV	Ultra-violet
TOA	Top of atmosphere
PM	Particulate matter
CALIOP	Cloud-Aerosol Lidar with Orthogonal Polarization
CALIPSO	Cloud-Aerosol Lidar and Infrared Pathfinder Satellite Observation
SNR	Signal-to-noise ratio
DOFS	Degrees of freedom for signal
PBL(H)	Planetary boundary layer (height)
CLARS-FTS	California Laboratory for Atmospheric Remote Sensing Fourier Transform Spectrometer
ALH	Aerosol layer height
IR	Infrared
AOCH	Aerosol optical central height
AEH	Aerosol effective height
SCIAMACHY	Scanning Imaging Absorption spectroMeter for Atmospheric CHartographY
TROPOMI	TROPOspheric Monitoring Instrument
EPIC	Earth Polychromatic Imaging Camera
DSCOVR	Deep Space Climate Observatory
GEMS	Geostationary Environment Monitoring Spectrometer
OMI	Ozone Monitoring Instrument
UVAI	UV aerosol index

DOAS	Differential optical absorption spectroscopy
SZA	Solar zenith angle
SCD	Slant column density
LUT	Look-up table
VisAI	Visible aerosol index
HAF	Highly absorbing fine
NA	Non-absorbing
AERONET	AErosol RObotic NETwork
RMSE	Root mean square error
MBE	Mean bias error
NIR	Near-infrared
AOCH	Aerosol optical central height
SWIR	Shortwave infrared
TOMS	Total Ozone Mapping Spectrometer
AE	Angstrom exponent
LST	Local solar time
MERRA-2	Modern-Era Retrospective Analysis for Research and Applications, Version 2
MPLNET	NASA Micro-Pulse Lidar Network

Code availability

675 Aerosol layer height and aerosol optical depth analysis codes are available at <https://doi.org/10.5281/zenodo.10408292>.

Data availability

TROPOMI AOCHE dataset used in this study can be found at <http://doi.org/10.5281/zenodo.10407271>. EPIC level 2 AOCHE data can be found at https://opendap.larc.nasa.gov/opendap/DSCOVER/EPIC/L2_AOCHE_01/contents.html. GEMS L2 AEH V2.0 and AERAOD V2.0 can be downloaded from the Environmental Satellite Center website (680 <https://nesc.nier.go.kr/en/html/datasvc/index.do>). CALIOP level 2 data are from <https://asdc.larc.nasa.gov/data/>. Earthdata registration is required for the access to the CALIOP level 2 data.

Author contribution

HK performed data curation, formal analysis, visualization, and writing most of the original draft. XC was responsible for conceptualization, formal analysis, methodology, writing parts of the original draft, and supervision. XC also provided (685 TROPOMI AOCHE data and ZL provided the EPIC AOCHE data. JW provided comments on the research design and supervision. MZ contributed on formal analysis and GRC provided comments on writing focus and structure. SSP provided GEMS AEH V2.0 data. All authors including JK provided comments and edited the manuscript.

Competing interests

Jun Wang is a member of the editorial board of *Atmospheric Measurement Techniques*.

690 Acknowledgements

This was supported by NASA EPIC/DSCOVER Science team program (80NSSC22K0503), NOAA (1305M322PNRMT0542, 1305M323PNRMN0450, NA23OAR4310303), and the NASA SERVIR grant (80NSSC23K0244). We thank the National Institute of Environmental Research of South Korea for providing GEMS satellite data. We acknowledge the public availability of CALIOP level 2 aerosol profile data from the NASA Langley Research Center Atmospheric Science Data Center. We thank (695 all Principal Investigators, Co-Principal Investigators and their staff for establishing and maintaining the AERONET sites used in this investigation.

References

- 700 Babu, S. S., Moorthy, K. K., Manchanda, R. K., Sinha, P. R., Satheesh, S. K., Vajja, D. P., Srinivasan, S., and Kumar, V. H. A.: Free tropospheric black carbon aerosol measurements using high altitude balloon: Do BC layers build "their own homes" up in the atmosphere?, *Geophys Res Lett*, 38, <https://doi.org/10.1029/2011gl046654>, 2011.
- Chang, D. and Song, Y.: Estimates of biomass burning emissions in tropical Asia based on satellite-derived data, *Atmos. Chem. Phys.*, 10, 2335-2351, <https://doi.org/10.5194/acp-10-2335-2010>, 2010.
- 705 Chen, X., Xu, X. G., Wang, J., and Diner, D. J.: Can multi-angular polarimetric measurements in the oxygen-A and B bands improve the retrieval of aerosol vertical distribution?, *J Quant Spectrosc Radiat*, 270, <https://doi.org/10.1016/j.jqsrt.2021.107679>, 2021a.
- Chen, X., Wang, J., Xu, X. G., Zhou, M., Zhang, H. X., Garcia, L. C., Colarco, P. R., Janz, S. J., Yorks, J., McGill, M., Reid, J. S., de Graaf, M., and Kondragunta, S.: First retrieval of absorbing aerosol height over dark target using TROPOMI oxygen B band: Algorithm development and application for surface particulate matter estimates, *Remote Sensing of Environment*, 265, 18, <https://doi.org/10.1016/j.rse.2021.112674>, 2021b.
- 710 Chimot, J., Veeffkind, J. P., Vlemmix, T., de Haan, J. F., Amiridis, V., Proestakis, E., Marinou, E., and Levelt, P. F.: An exploratory study on the aerosol height retrieval from OMI measurements of the 477 nm O₂-O₂ spectral band using a neural network approach, *Atmos Meas Tech*, 10, 783-809, <https://doi.org/10.5194/amt-10-783-2017>, 2017.
- Cho, Y., Kim, J., Go, S., Kim, M., Lee, S., Kim, M., Chong, H., Lee, W. J., Lee, D. W., Torres, O., and Park, S. S.: First Atmospheric Aerosol Monitoring Results from Geostationary Environment Monitoring Spectrometer (GEMS) over Asia[preprint], <https://doi.org/10.5194/amt-2023-221>, 23 October 2023.
- 715 Choi, M., Sander, S. P., Spurr, R. J. D., Pongetti, T. J., van Harten, G., Drouin, B. J., Diner, D. J., Crisp, D., Eldering, A., Kalashnikova, O. V., Jiang, J. H., Hyon, J. J., and Fu, D. J.: Aerosol profiling using radiometric and polarimetric spectral measurements in the O₂ near infrared bands: Estimation of information content and measurement uncertainties, *Remote Sensing of Environment*, 253, 20, <https://doi.org/10.1016/j.rse.2020.112179>, 2021.
- 720 Christian, K., Wang, J., Ge, C., Peterson, D., Hyer, E., Yorks, J., and McGill, M.: Radiative Forcing and Stratospheric Warming of Pyrocumulonimbus smoke Aerosols: First Modeling Results With Multisensor (EPIC, CALIPSO, AND CATS) Views from Space, *Geophys Res Lett*, 46, 10061-10071, <https://doi.org/10.1029/2019gl082360>, 2019.
- Ding, S. G., Wang, J., and Xu, X. G.: Polarimetric remote sensing in oxygen A and B bands: sensitivity study and information content analysis for vertical profile of aerosols, *Atmos Meas Tech*, 9, 2077-2092, <https://doi.org/10.5194/amt-9-2077-2016>, 2016.
- 725 Geddes, A. and Bösch, H.: Tropospheric aerosol profile information from high-resolution oxygen A-band measurements from space, *Atmos Meas Tech*, 8, 859-874, <https://doi.org/10.5194/amt-8-859-2015>, 2015.
- Geogdzhayev, I. V. and Marshak, A.: Calibration of the DSCOVR EPIC visible and NIR channels using MODIS Terra and Aqua data and EPIC lunar observations, *Atmos. Meas. Tech.*, 11, 359-368, <https://doi.org/10.5194/amt-11-359-2018>, 2018.
- 730 Kang, M., Ahn, M.-H., Liu, X., Jeong, U., and Kim, J.: Spectral Calibration Algorithm for the Geostationary Environment Monitoring Spectrometer (GEMS), *Remote Sens-Basel*, 12, 2846, 2020.
- Kim, J., Jeong, U., Ahn, M. H., Kim, J. H., Park, R. J., Lee, H., Song, C. H., Choi, Y. S., Lee, K. H., Yoo, J. M., Jeong, M. J., Park, S. K., Lee, K. M., Song, C. K., Kim, S. W., Kim, Y. J., Kim, S. W., Kim, M., Go, S., Liu, X., Chance, K., Chan Miller, C., Al-Saadi, J., Veihelmann, B., Bhartia, P. K., Torres, O., Abad, G. G., Haffner, D. P., Ko, D. H., Lee, S. H., Woo, J. H., Chong, H., Park, S. S., Nicks, D., Choi, W. J., Moon, K. J., Cho, A., Yoon, J., Kim, S. K., Hong, H., Lee, K., Lee, H., Lee, S., Choi, M., Veeffkind, P., Levelt, P. F., Edwards, D. P., Kang, M., Eo, M., Bak, J., Baek, K., Kwon, H. A., Yang, J., Park, J., Han, K. M., Kim, B. R., Shin, H. W., Choi, H., Lee, E., Chong, J., Cha, Y., Koo, J. H., Irie, H., Hayashida, S., Kasai, Y., Kanaya, Y., Liu, C., Lin, J., Crawford, J. H., Carmichael, G. R., Newchurch, M. J., Lefter, B. L., Herman, J. R., Swap, R. J., Lau, A. K. H., Kurosu, T. P., Jaross, G., Ahlers, B., Dobber, M., McElroy, C. T., and Choi, Y.: New Era of Air Quality Monitoring from Space: Geostationary Environment Monitoring Spectrometer (GEMS), *B Am Meteorol Soc*, 101, E1-E22, <https://doi.org/10.1175/bams-d-18-0013.1>, 2020.
- 740 Kim, M., Kim, J., Lim, H., Lee, S., Cho, Y., Yeo, H., and Kim, S. W.: Exploring geometrical stereoscopic aerosol top height retrieval from geostationary satellite imagery in East Asia, *Atmos Meas Tech*, 16, 2673-2690, <https://doi.org/10.5194/amt-16-2673-2023>, 2023.
- Kim, M., Kim, J., Torres, O., Ahn, C., Kim, W., Jeong, U., Go, S., Liu, X., Moon, K. J., and Kim, D. R.: Optimal Estimation-Based Algorithm to Retrieve Aerosol Optical Properties for GEMS Measurements over Asia, *Remote Sens-Basel*, 10, <https://doi.org/10.3390/rs10020162>, 2018.
- 745 Kipling, Z., Stier, P., Schwarz, J. P., Perring, A. E., Spackman, J. R., Mann, G. W., Johnson, C. E., and Telford, P. J.: Constraints on aerosol processes in climate models from vertically-resolved aircraft observations of black carbon, *Atmos Chem Phys*, 13, 5969-5986, <https://doi.org/10.5194/acp-13-5969-2013>, 2013.
- Kipling, Z., Stier, P., Johnson, C. E., Mann, G. W., Bellouin, N., Bauer, S. E., Bergman, T., Chin, M., Diehl, T., Ghan, S. J., Iversen, T., Kirkevåg, A., Kokkola, H., Liu, X. H., Luo, G., van Noije, T., Pringle, K. J., von Salzen, K., Schulz, M., Seland, O., Skeie, R. B., Takemura, T., Tsigaridis, K., and Zhang, K.: What controls the vertical distribution of aerosol? Relationships between process sensitivity in HadGEM3-UKCA and inter-model variation from AeroCom Phase II, *Atmos Chem Phys*, 16, 2221-2241, <https://doi.org/10.5194/acp-16-2221-2016>, 2016.
- 750 Kleipool, Q., Ludewig, A., Babić, L., Bartstra, R., Braak, R., Dierssen, W., Dewitte, P. J., Kenter, P., Landzaat, R., Leloux, J., Loots, E., Meijering, P., van der Plas, E., Rozemeijer, N., Schepers, D., Schiavini, D., Smeets, J., Vacanti, G., Vonk, F., and Veeffkind, P.: Pre-launch calibration results of the TROPOMI payload on-board the Sentinel-5 Precursor satellite, *Atmos. Meas. Tech.*, 11, 6439-6479, <https://doi.org/10.5194/amt-11-6439-2018>, 2018.
- Koch, D. and Del Genio, A. D.: Black carbon semi-direct effects on cloud cover: review and synthesis, *Atmos Chem Phys*, 10, 7685-7696, <https://doi.org/10.5194/acp-10-7685-2010>, 2010.
- 760 Koffi, B., Schulz, M., Breon, F. M., Dentener, F., Steensen, B. M., Griesfeller, J., Winker, D., Balkanski, Y., Bauer, S. E., Bellouin, N., Bernsten, T., Bian, H. S., Chin, M., Diehl, T., Easter, R., Ghan, S., Hauglustaine, D. A., Iversen, T., Kirkevåg, A., Liu, X. H., Lohmann, U., Myhre, G., Rasch, P., Seland, O., Skeie, R. B., Steenrod, S. D., Stier, P., Tackett, J., Takemura, T., Tsigaridis, K., Vuolo, M. R., Yoon, J., and Zhang, K.: Evaluation of the aerosol vertical distribution in global aerosol models through comparison against CALIOP measurements: AeroCom phase II results, *J Geophys Res-Atmos*, 121, 7254-7283, <https://doi.org/10.1002/2015jd024639>, 2016.
- 765 Kokhanovsky, A. A. and Rozanov, V. V.: The determination of dust cloud altitudes from a satellite using hyperspectral measurements in the gaseous absorption band, *Int J Remote Sens*, 31, 2729-2744, <https://doi.org/10.1080/01431160903085644>, 2010.

- Lee, L., Zhang, J., Reid, J. S., and Yorks, J. E.: Investigation of CATS aerosol products and application toward global diurnal variation of aerosols, *Atmos. Chem. Phys.*, 19, 12687-12707, <https://doi.org/10.5194/acp-19-12687-2019>, 2019.
- 770 Lu, Z. D., Wang, J., Xu, X. G., Chen, X., Kondragunta, S., Torres, O., Wilcox, E. M., and Zeng, J.: Hourly Mapping of the Layer Height of Thick Smoke Plumes Over the Western US in 2020 Severe Fire Season, *Front. Remote Sens.*, 2, 13, <https://doi.org/10.3389/frsen.2021.766628>, 2021.
- Lu, Z. D., Wang, J., Chen, X., Zeng, J., Wang, Y., Xu, X. G., Christian, K. E., Yorks, J. E., Nowottnick, E. P., Reid, J. S., and Xian, P.: First Mapping of Monthly and Diurnal Climatology of Saharan Dust Layer Height Over the Atlantic Ocean From EPIC/DSCOVR in Deep Space, *Geophys Res Lett*, 50, 10, <https://doi.org/10.1029/2022gl102552>, 2023.
- 775 Marshak, A., Herman, J., Szabo, A., Blank, K., Carn, S., Cede, A., Geogdzhayev, I., Huang, D., Huang, L. K., Knyazikhin, Y., Kowalewski, M., Krotkov, N., Lyapustin, A., McPeters, R., Meyer, K. G., Torres, O., and Yang, Y. K.: Earth Observations from DSCOVR EPIC Instrument, *B Am Meteorol Soc*, 99, 1829-1850, <https://doi.org/10.1175/Bams-D-17-0223.1>, 2018.
- Muller, J. P., Denis, M. A., Dundas, R. D., Mitchell, K. L., Naud, C., and Mannstein, H.: Stereo cloud-top heights and cloud fraction retrieval from ATSR-2, *Int J Remote Sens*, 28, 1921-1938, <https://doi.org/10.1080/01431160601030975>, 2007.
- 780 Nanda, S., de Graaf, M., Veeffkind, J. P., Sneep, M., ter Linden, M., Sun, J. Y. T., and Levelt, P. F.: A first comparison of TROPOMI aerosol layer height (ALH) to CALIOP data, *Atmos Meas Tech*, 13, 3043-3059, <https://doi.org/10.5194/amt-13-3043-2020>, 2020.
- Park, S. S., Kim, J., Lee, H., Torres, O., Lee, K. M., and Lee, S. D.: Utilization of O-4 slant column density to derive aerosol layer height from a space-borne UV-visible hyperspectral sensor: sensitivity and case study, *Atmos Chem Phys*, 16, 1987-2006, <https://doi.org/10.5194/acp-16-1987-2016>, 2016.
- 785 Park, S. S., Kim, J., Cho, Y., Lee, H., Park, J., Lee, D. W., Lee, W. J., and Kim, D. R.: Retrieval Algorithm for Aerosol Effective Height from the Geostationary Environment Monitoring Spectrometer (GEMS)[preprint], <https://doi.org/10.5194/amt-2023-136>, 04 July 2023.
- Peterson, D., Hyer, E., and Wang, J.: Quantifying the potential for high-altitude smoke injection in the North American boreal forest using the standard MODIS fire products and subpixel-based methods, *J Geophys Res-Atmos*, 119, 3401-3419, <https://doi.org/10.1002/2013jd021067>, 2014.
- 790 Pierangelo, C., Chedin, A., Heilliette, S., Jacquinet-Husson, N., and Armante, R.: Dust altitude and infrared optical depth from AIRS, *Atmos Chem Phys*, 4, 1813-1822, <https://doi.org/10.5194/acp-4-1813-2004>, 2004.
- Rao, L. L., Xu, J., Efremenko, D. S., Loyola, D. G., and Doicu, A.: Hyperspectral Satellite Remote Sensing of Aerosol Parameters: Sensitivity Analysis and Application to TROPOMI/S5P, *Front. Environ. Sci.*, 9, 16, <https://doi.org/10.3389/fenvs.2021.770662>, 2022.
- 795 Reid, J. S., Kinney, J. E., Westphal, D. L., Holben, B. N., Welton, E. J., Tsay, S.-C., Eleuterio, D. P., Campbell, J. R., Christopher, S. A., Colarco, P. R., Jonsson, H. H., Livingston, J. M., Maring, H. B., Meier, M. L., Pilewskie, P., Prospero, J. M., Reid, E. A., Remer, L. A., Russell, P. B., Savoie, D. L., Smirnov, A., and Tanré, D.: Analysis of measurements of Saharan dust by airborne and ground-based remote sensing methods during the Puerto Rico Dust Experiment (PRIDE), *Journal of Geophysical Research: Atmospheres*, 108, <https://doi.org/https://doi.org/10.1029/2002JD002493>, 2003.
- 800 Shi, Y. S., Sasai, T., and Yamaguchi, Y.: Spatio-temporal evaluation of carbon emissions from biomass burning in Southeast Asia during the period 2001-2010, *Ecol Model*, 272, 98-115, <https://doi.org/10.1016/j.ecolmodel.2013.09.021>, 2014.
- Spurr, R. and Christi, M.: On the generation of atmospheric property Jacobians from the (V)LIDORT linearized radiative transfer models, *J Quant Spectrosc Ra*, 142, 109-115, <https://doi.org/10.1016/j.jqsrt.2014.03.011>, 2014.
- 805 Stein
Zweers, D. C.: TROPOMI ATBD of the UV aerosol index, S5P-KNMI-L2-0008-RP: <https://sentinel.esa.int/documents/247904/2476257/Sentinel-5P-TROPOMI-ATBD-UV-Aerosol-Index.pdf>, last access: 17 December 2023.
- Torres, O., Bhartia, P. K., Herman, J. R., Ahmad, Z., and Gleason, J.: Derivation of aerosol properties from satellite measurements of backscattered ultraviolet radiation: Theoretical basis, *J Geophys Res-Atmos*, 103, 17099-17110, <https://doi.org/10.1029/98jd00900>, 1998.
- 810 Torres, O., Tanskanen, A., Veihelmann, B., Ahn, C., Braak, R., Bhartia, P. K., Veeffkind, P., and Levelt, P.: Aerosols and surface UV products from Ozone Monitoring Instrument observations: An overview, *J Geophys Res-Atmos*, 112, <https://doi.org/10.1029/2007jd008809>, 2007.
- Vandenbussche, S., Kochenova, S., Vandaele, A. C., Kumps, N., and De Maziere, M.: Retrieval of desert dust aerosol vertical profiles from IASI measurements in the TIR atmospheric window, *Atmos Meas Tech*, 6, 2577-2591, <https://doi.org/10.5194/amt-6-2577-2013>, 2013.
- 815 Wang, J. and Christopher, S. A.: Intercomparison between satellite-derived aerosol optical thickness and PM_{2.5} mass: Implications for air quality studies, *Geophys Res Lett*, 30, <https://doi.org/10.1029/2003gl018174>, 2003.
- Wang, J. and Christopher, S. A.: Mesoscale modeling of Central American smoke transport to the United States: 2. Smoke radiative impact on regional surface energy budget and boundary layer evolution, *J Geophys Res-Atmos*, 111, <https://doi.org/10.1029/2005jd006720>, 2006.
- 820 Wang, J., Christopher, S. A., Nair, U. S., Reid, J. S., Prins, E. M., Szykman, J., and Hand, J. L.: Mesoscale modeling of Central American smoke transport to the United States: 1. "Top-down" assessment of emission strength and diurnal variation impacts, *J Geophys Res-Atmos*, 111, <https://doi.org/10.1029/2005jd006416>, 2006.
- 825 Wang, J., Ge, C., Yang, Z. F., Hyer, E. J., Reid, J. S., Chew, B. N., Mahmud, M., Zhang, Y. X., and Zhang, M. G.: Mesoscale modeling of smoke transport over the Southeast Asian Maritime Continent: Interplay of sea breeze, trade wind, typhoon, and topography, *Atmos Res*, 122, 486-503, <https://doi.org/10.1016/j.atmosres.2012.05.009>, 2013.
- Wang, J., Roudini, S., Hyer, E. J., Xu, X. G., Zhou, M., Garcia, L. C., Reid, J. S., Peterson, D. A., and da Silva, A. M.: Detecting nighttime fire combustion phase by hybrid application of visible and infrared radiation from Suomi NPP VIIRS, *Remote Sensing of Environment*, 237, 14, <https://doi.org/10.1016/j.rse.2019.111466>, 2020.
- 830 Wendisch, M., Hellmuth, O., Ansmann, A., Heintzenberg, J., Engelmann, R., Althausen, D., Eichler, H., Wuller, D., Hu, M., Zhang, Y., and Mao, J.: Radiative and dynamic effects of absorbing aerosol particles over the Pearl River Delta, China, *Atmos Environ*, 42, 6405-6416, <https://doi.org/10.1016/j.atmosenv.2008.02.033>, 2008.
- Winker, D. M., Tackett, J. L., Getzewich, B. J., Liu, Z., Vaughan, M. A., and Rogers, R. R.: The global 3-D distribution of tropospheric aerosols as characterized by CALIOP, *Atmos Chem Phys*, 13, 3345-3361, <https://doi.org/10.5194/acp-13-3345-2013>, 2013.
- 835 Wu, L. H., Hasekamp, O., van Diedenhoven, B., Cairns, B., Yorks, J. E., and Chowdhary, J.: Passive remote sensing of aerosol layer height using near-UV multiangle polarization measurements, *Geophys Res Lett*, 43, 8783-8790, <https://doi.org/10.1002/2016gl069848>, 2016.

- 840 Xu, X., Wang, J., Wang, Y., and Kokhanovsky, A.: Chapter 1 - Passive Remote Sensing of Aerosol Height, in: Remote Sensing of Aerosols, Clouds, and Precipitation, edited by: Tanvir Islam, Y. H., Alexander Kokhanovsky, Jun Wang, Elsevier, Cambridge, MA, 1-22, <https://doi.org/10.1016/B978-0-12-810437-8.00001-3>, 2018.
- Xu, X. G., Wang, J., Wang, Y., Zeng, J., Torres, O., Reid, J. S., Miller, S. D., Martins, J. V., and Remer, L. A.: Detecting layer height of smoke aerosols over vegetated land and water surfaces via oxygen absorption bands: hourly results from EPIC/DSCOVR in deep space, *Atmos Meas Tech*, 12, 3269-3288, <https://doi.org/10.5194/amt-12-3269-2019>, 2019.
- 845 Xu, X. G., Wang, J., Wang, Y., Zeng, J., Torres, O., Yang, Y. K., Marshak, A., Reid, J., and Miller, S.: Passive remote sensing of altitude and optical depth of dust plumes using the oxygen A and B bands: First results from EPIC/DSCOVR at Lagrange-1 point, *Geophys Res Lett*, 44, 7544-7554, <https://doi.org/10.1002/2017gl073939>, 2017.
- Yang, Z. F., Wang, J., Ichoku, C., Hyer, E., and Zeng, J.: Mesoscale modeling and satellite observation of transport and mixing of smoke and dust particles over northern sub-Saharan African region, *J Geophys Res-Atmos*, 118, 12139-12157, <https://doi.org/10.1002/2013jd020644>, 2013.
- 850 Zeng, J., Han, Q. Y., and Wang, J.: High-spectral resolution simulation of polarization of skylight: Sensitivity to aerosol vertical profile, *Geophys Res Lett*, 35, <https://doi.org/10.1029/2008gl035645>, 2008.
- Zhang, L., Li, Q. B., Gu, Y., Liou, K. N., and Meland, B.: Dust vertical profile impact on global radiative forcing estimation using a coupled chemical-transport-radiative-transfer model, *Atmos Chem Phys*, 13, 7097-7114, <https://doi.org/10.5194/acp-13-7097-2013>, 2013.

855